Assessment of a numerical model to reproduce event-scale erosion and deposition distributions in a braided river

R.D. Williams[1], R. Measures[2], M. Hicks[2], J. Brasington[3]

[1]School of Geographical and Earth Sciences, University of Glasgow, Main Building, East Quadrangle, G12 8QQ, United Kingdom, richard.williams@glasgow.ac.uk.

[2]National Institute of Water and Atmospheric Research, PO Box 8602, Christchurch, 8011, New Zealand.

[3]School of Geography, Queen Mary, University of London, London, E1 4NS, United Kingdom.

Key findings

Calibration of morphological model with DEMs of Difference from a natural river

Validation of Gaeuman et al. mixed grain size bedload formula for reach-scale application

Sensitivity of unsteady flow simulations to morphological acceleration factor

Abstract

Numerical morphological modelling of braided rivers, using a physics-based approach, is increasingly used as a technique to explore controls on river pattern and, from an applied perspective, to simulate the impact of channel modifications. This paper assesses a depth averaged non-uniform sediment model (Delft3D) to predict the morphodynamics of a 2.5 km long reach of the braided Rees River, New Zealand, during a single high-flow event. Evaluation of model performance primarily focused upon using high-resolution Digital Elevation Models (DEMs) of Difference, derived from a fusion of terrestrial laser scanning and optical empirical bathymetric mapping, to compare observed and predicted patterns of erosion and deposition, and reach scale sediment budgets. For the calibrated model, this was supplemented with planform metrics (e.g. braiding intensity). Extensive sensitivity analysis of model functions and parameters was executed, including consideration of numerical scheme for bedload component calculations, hydraulics, bed composition, bedload transport and bed slope effects, bank erosion and frequency of calculations. Total predicted volumes of erosion and deposition corresponded well to those observed. The difference between predicted and observed volumes of erosion was less than the factor of two that characterises the accuracy of the Gaeuman et al. bedload transport formula. Grain size distributions were best represented using two-phi intervals. For unsteady flows, results were sensitive to the morphological time scale factor. The

approach of comparing observed and predicted morphological sediment budgets shows the value of using natural experiment datasets for model testing. Sensitivity results are transferable to guide Delft3D applications to other rivers.

1 Introduction

Morphological models of braided rivers are used as tools for exploration, explanation and prediction. A variety of modelling frameworks have been applied to simulate braided river morphodynamics [*Williams et al.*, 2016], spanning from reduced-complexity [e.g. *Murray and Paola*, 1994; 2003] to reductionist approaches [e.g. *Nicholas*, 2013c]. From the perspective of environmental management, particularly applied engineering practice, there is interest in developing morphodynamic models that can be used to support river management decisions [e.g. *Karmaker and Dutta*, 2016]. For example, those concerned with limiting ecosystem degradation, and managing flood and geomorphological hazards. Such applications demand models that can simulate three-dimensional morphodynamics at the reach spatial scale [reach lengths of 10 to 100 river widths; *Ferguson*, 2007] over annual to centennial timescales. Two-dimensional (2D), physics-based [sensu *Nicholas*, 2013b] models have potential for simulating qualitative planform characteristics of braided rivers [*Jang and Shimizu*, 2005; *Kleinhans*, 2010; *Lotsari et al.*, 2013; *Nicholas*, 2013a; c; *Schuurman et al.*, 2013; *Schuurman and Kleinhans*, 2015]. Although morphodynamic modelling with graded sediment has been used in many studies, there has only been limited testing with laboratory data [*Sun et al.*,2015] and in synthetic river settings [*Yang et al.*, 2015]. Graded sediment morphodynamic models have not been evaluated using high resolution topographic data from a natural river.

1.1 Model assessment using natural experiment datasets

In an ideal world, assessment of braided river morphodynamic model predictions would be made using spatially and temporally distributed data on hydrodynamics, sediment flux and bed level. This would enable the calibration of numerous parameters associated with morphodynamic physics-based models [*Knight*, 2013; *Church and Ferguson*, 2015]. Unfortunately, logistical and technological constraints limit the feasibility of acquiring such data. With respect to observing bed level change, a revolution in geospatial technologies has enabled the monitoring of fluvial morphology at unprecedented resolution and accuracy [*Carbonneau and Piégay*, 2012; *Tarolli*, 2014; *Passalacqua et al.*, 2015]. Whilst the timing of topographic surveys is still constrained to low flow conditions, the availability of high-resolution topography enables the testing of model predictions to extend beyond planimetric comparisons of morphological features, such as riffles, pools and bars, to post-hoc analysis using DEMs of Difference [DoD; *Wheaton et al.*, 2010]. A limited number of natural experiment [*Tucker*, 2009] datasets demonstrate the efficacy of using sequences of pre- and post-event DEMs to map morphological change in braided rivers [e.g. *Carrivick et al.*, 2012; *Lallias-Tacon et al.*, 2014; *Lane et al.*, 2003; *Lane et al.*, 2010; Milan et al., 2007; *Moretto et al.*, 2014; *Wheaton et al.*, 2010; *Williams et al.*, 2011]. Such datasets are, however, only useful for the purposes of testing morphodynamic numerical models if a flow record is available during the monitoring period.

1.2 2D physics-based modelling

The development of 2D numerical morphodynamic models has been challenged by problems associated with the general inaccuracy of sediment transport formulas, the parameterisation or

exclusion of relevant processes, spatial and temporal discretisation, high computational overheads of calculations, and the sensitivity of simulation results to small errors in initial and boundary conditions. Investigations have tested steady-state shallow-water predictions of natural braided river hydrodynamics, using high-resolution topographic surveys for boundary conditions, spatially distributed surveys of depth and velocity, and time-lapse and aerial photography of inundation extent [*Hicks et al.*, 2006; *Jowett and Duncan*, 2012; *Nicholas et al.*, 2012; *Williams et al.*, 2013; *Javernick et al.*, 2016].

Nicholas [2013a; 2013c] demonstrates how changes to key parameters in a 2D morphodynamic model can vary the river style that emerges after centennial-scale model simulations. This work indicates the potential of a 2D physics-based approach for investigating controls on river pattern but the primary focus was upon simulation of virtual rather than real rivers. The exception to this is a simulation of a braided reach, based upon the Waimakariri River [*Nicholas*, 2013c]. Visual comparisons between predicted and natural river planform indicate qualitative similarity but topographic relief is greater than that observed. This was attributed to the assumption of a single grain size and thus a lack of bed armour development. A similar approach of using a braided river's broad characteristics to set up virtual models is used by *Kleinhans* [2010] for the River Rhone and *Crosato and Saleh* [2011] for the Allier River. *Xia et al.* [2013] developed a model of the Lower Yellow River but their analysis of morphological change is restricted to a number of repeat cross-section surveys. *Lotsari et al.* [2013] simulated one year of morphological change along the sand-bed lower Tana River. Morphological predictions were compared to an annual DoD but the survey data were relatively sparse and considerable scaling was required to match observed volumes of erosion and deposition. In a laboratory

97 environment, *Jang and Shimizu* [2005] demonstrate how topographic survey data can be used
98 to assess model predictions. *Ziliani et al.* [2013] use a reduced-complexity model to simulate
99 the morphodynamics of the Tagliamento River, through multiple flood events. Airborne LiDAR
100 was used for initial topography but this did not include a representation of bed levels in
101 inundated areas, which comprised 30% of braidplain area. Moreover, a repeat topographic
102 survey was not available at the end of the high-flow event series so evaluation relied solely
103 upon the use of the aerial imagery.

104 The preceding review of applications of morphodynamic models to real rivers indicates that
105 there is considerable scope to enhance model assessment, particularly for models simulating
106 graded sediment. Robust calibration can draw upon a variety of observational data, driven by
107 modelling objectives. For the case of simulating the morphodynamics of natural rivers, model
108 testing needs to consider the affinity between observed and predicted patterns of erosion and
109 deposition. Coupled with this, there is also a need to test whether the correct mass of sediment
110 is being transported at the spatially aggregated reach scale. Whilst observed DoDs provide a
111 new opportunity for performance evaluation, the understanding of parameter sensitivity in
112 graded sediment braided river morphodynamic models is in its infancy. For a sand bed river,
113 *Schuurman et al.* [2013] presents a sensitivity analysis of a depth-averaged Delft3D
114 morphodynamic model. Their results showed marginal sensitivity to morphological
115 acceleration, and initial and boundary conditions, but showed more sensitivity to bed
116 roughness, sediment transport relation and bed slope effect. To guide future model
117 applications, such analysis is needed for gravel-bed braided rivers, where predictions will be
118 sensitive to bank erosion, grain-size composition and fractional transport.

1.3 Aim and structure

This paper aims to evaluate the performance of a physics-based model to predict natural, reach-scale, braided river morphodynamics for a single high-flow event. The following section introduces the study site, observed morphological data and numerical modelling methodology, including an overview of Delft3D, model setup and the method used to compare observed and predicted morphology. Next, the details and results of a two stage modelling workflow are described: (i) one-at-a-time sensitivity analysis to test model functions and parameters; and (ii) model tuning and assessment of model performance. The final section discusses the parameter sensitivity analysis and the use of natural experiment data for model assessment.

2 Study site and methodology

2.1 Study site and observational data

This paper uses a natural experiment dataset that was acquired as part of the ReesScan project [*Brasington*, 2010; *Williams et al.*, 2011]. The 402 km^2 Rees catchment is located east of New Zealand's Southern Alps and discharges into Lake Wakatipu at 44.85°S, 168.38°E. Catchment geomorphology is described by *Cook et al.* [2014], *Williams et al.* [2013] and *Williams* [2014]. In this paper the morphodynamics of a 2.5 km long study reach of the Rees River (Figure 1a) are modelled. Hydraulic modelling of this reach is reported by *Williams et al.* [2013]. The reach is characterised by transport-limited conditions [*Montgomery and Buffington*, 1997] and a longitudinal bed slope of 0.005.

A flow record was derived from a rated gauge 8 km upstream from the study site. During 2010 the mean catchment runoff was 2500 mm. This paper focuses upon simulating an unsteady event with peak discharge of 227 m^3s^{-1} (Figure 2). Aerially exposed and inundated braidplain areas were surveyed before and after the event using a fusion of TLS and optical-empirical bathymetric mapping [*Williams et al.*, 2014; Figure 1]. A DoD was calculated using an error analysis approach that subjected the DEMs to probabilistic thresholding [*Brasington et al.*, 2003], using a Confidence Interval of 87%. This approach aims to ensure that DoDs are reliable, by distinguishing between real morphological change and noise. Errors in each DEM were characterised by the Standard Deviation Error associated with the source of elevation data. Constant values were used for three categories: gravelly areas surveyed by TLS; vegetated areas surveyed by TLS; or inundated areas mapped using bathymetric mapping.

The sedimentology of the study reach was measured by sampling the surface (28 samples), surface layer (3 samples) and subsurface (4 samples; Figure 3). Surface distributions were sampled by means of a 100 clast grid-count technique that is equivalent to the *Wolman* [1954] pebble count approach. Surface layer sampling followed *Klingeman et al.* [1979] and *Klingeman and Emmett's* [1982] method, where material is removed to the depth of the largest clast on a bar and around a radius equal to 10x the largest clast's long-axis. Subsurface sampling followed *Church et al.'s* [1987] practical criterion of weighing 100x the weight of the largest surface clast on the bar of interest. The depth of each sample hole was determined by estimating the thickness of the most recently deposited sediment layer. Both volumetric samples were acquired from sites located on active bar surfaces. Particle-size ranges are described using the terminology of *Blott and Pye* [2001].

2.2 Delft3D

Open source Delft3D modelling software (revision 1301, based on release version FLOW4.00.07) was used to simulate depth-averaged hydro- and morpho-dynamics. This version incorporates a slope based bank erosion algorithm and three bedload transport equations that were coded by the authors; these are elaborated upon below. *Lesser et al.* [2004] and *Deltares* [2011] provide a full description of the hydrodynamic equations and morphodynamic updating scheme, and *Sloff and Mosselman* [2012, and references therein] summarise the model's historical development. The Delft3D modelling system has been widely applied in depth-averaged mode to simulate interactions between flow, sediment transport and morphology. The Navier Stokes equations were solved using shallow water assumptions and the Boussinesq approximation [*van der Wegen and Roelvink*, 2008]. Shallow water equations were solved using an Alternating Direction Implicit method and the horizontal advection terms were spatially discretized using a Cyclic method [*Stelling and Leendertse*, 1992]. The Exner equation was used to calculate changes in bed elevation as a function of bedload flux in or out of a cell. Since a multi-grain size approach was adopted, the Exner equation was applied for each grain size fraction, at each morphological timestep. The bed was divided into a constant thickness surface active layer which was underlain by underlayers above a nonerodible layer. All sediment in the active layer was assumed to be well mixed and was subject to exchange with sediment in transport [*Hirano*, 1971]. Dissolved and suspended sediment loads were not modelled because bedload is the key control on gravel-bed braided river morphology [*Leopold*, 1992].

Two bank erosion schemes were tested: the *ThetSD* scheme that allows the partial redistribution of erosion from a wet cell to adjacent dry cells [*van der Wegen et al.*, 2008; *Deltares*, 2011]; and a *repose* scheme that specifies the repose gradient above which slope failure will occur. For the repose scheme the slope across each cell boundary was calculated and material was moved down slope in locations where the slope angle exceeds the repose slope. Net slope angle and orientation across each boundary was calculated (including slope parallel to, as well as normal to the cell boundary) to make the scheme relatively independent of grid cell orientation. The flux of material from the active layer was based upon how much the slope is exceeded and the orientation of the slope relative to the cell boundary. Due to the generally low relief of braided rivers, the slope achieved at eroding banks in the model is generally resolution sensitive because the horizontal distance from the base to top of banks in the natural river is generally finer than the resolution of the model.

2.3 Model setup

The extent of the curvilinear model grid is shown in Figure 1a. Gradients in width-length ratios and cell sizes were minimised, and an automatic orthogonalization procedure was used to reduce deviations from orthogonality of lines between adjacent cell midpoints. The grid was smoothly curved over its length to follow the overall braidplain but no attempt was made to make the cells follow individual braids or topographic features. Grid cells for all simulations, except those that considered grid cell sensitivity, had an average length of 3 m.

199 The hydrograph recorded at the Invincible gauging station (8 km upstream of the study site)
200 was applied at the upstream flow boundary. At each hydraulic timestep, flow was divided
201 between the upstream row of cells using a total discharge boundary, which distributes flow
202 based on local flow depth, cell width and roughness. Sediment input at the upstream boundary
203 was calculated using the same bedload transport formula that was used to calculate transport
204 across the rest of the model domain. Input at the upstream boundary was therefore equal to
205 the flow's local sediment transport capacity and thus assumes transport-limited conditions
206 within the reach. Bed level and composition were fixed across the most upstream row of cells.
207 The downstream hydraulic boundary was a water level boundary based upon a rating curve
208 that was constructed by calculating normal depth at the downstream boundary cross section,
209 assuming a longitudinal water slope equal to the mean longitudinal bed gradient and constant
210 bed roughness equal to that set across the model domain. The water level across the
211 downstream boundary was assumed to be horizontal. Bed level change was allowed to occur
212 along the most downstream row of cells but the downstream water level boundary rating curve
213 was not updated. Under conditions of degradation a backwater effect will be caused; under
214 conditions of aggradation artificially low flow depths will be predicted. Either way, the
215 downstream boundary discourages morphological change because if bed levels at the boundary
216 lower then flow will deepen and encourage deposition, and vice versa. At the timescale of a
217 single high-flow event the sensitivity of the hydraulic predictions to relatively small variations in
218 the bed level of the downstream boundary were not considered to be significant. The timestep
219 was set to a Courant number less than 10. The minimum depth for sediment transport
220 calculations was set to 0.1 m. Each simulation was initiated with a 2 hour long hydraulic spin-up

with no morphological updating to allow the model to generate a stable and realistic hydraulic solution everywhere prior to starting morphological calculations.

2.4 Model assessment

Four approaches were used to compare observed and predicted morphological change. First, a quantitative comparison of total volumes of erosion and deposition, and the net volumetric change, was undertaken for each high-flow event. The observed morphological change was calculated using a DoD, which was subjected to probabilistic thresholding (Section 2.1). Vertical changes in the range from -0.05 to 0.05 m were excluded from the budgets for both observed and predicted morphological change. Second, the area of bed experiencing morphological change was plotted on a histogram. Third, the spatial distribution of erosion and deposition was plotted. The correspondence between the DoDs could then be qualitatively compared; this was particularly useful for comparing simulations during sensitivity analysis. Fourth, cross sections of morphological change were plotted for sensitivity analysis simulations that consider the numerical scheme and bank erosion algorithms. For all comparisons, modelled and predicted changes were calculated at the same spatial resolution.

A one-at-a-time (OAT) sensitivity analysis was adopted for the sensitivity analysis so that the results can be easily interpreted and used to guide parameterisation of other Delft3d models. Other approaches to sensitivity analysis could, however, be adopted in other applications guided by the results presented here. For example, a sensitivity analysis could be undertaken using an elementary effects (winding stairs) method [*Saltelli and Annoni*, 2010].

Following sensitivity analysis, the model was tuned. In additional to comparing observed and predicted morphological change, this model was also tested by comparing observed and predicted morphological units. This was achieved by running a hydrodynamic simulation using the observed and predicted post-event DEMs. A flow of 100 m^3s^{-1} was used for this testing because this flow yielded the highest braiding intensity, and thus planimetric morphological complexity, across the observed post-event DEM. The inundation area was classified as wet/dry to define the boundaries of bars. The following metrics were then calculated: channel count braiding intensity [*Howard et al.*, 1970]; confluence node density [*Ferguson*, 1993]; and the power relationships between bar perimeter and bar area, bar length and bar width, and bar convex perimeter and bar perimeter [*Kelly*, 2006; *van der Werff and van der Meer*, 2008].

Thirty-eight simulations were run to produce a baseline model that yielded reasonable morphological predictions (Table 1). This model featured a single active layer and a single underlayer. The assumption of a single underlayer was deemed adequate for simulation of a single high-flow event where the depth of scour was not expected to exceed the initial thickness of the underlayer. To reduce the computational time for the sensitivity analysis, the baseline model was used to determine the time period when most morphological change occurred (Figure 2). The rate of morphological change decreased significantly once discharge fell to c. 80 m^3s^{-1} so the subsequent sensitivity analysis simulations were stopped at this discharge threshold.

3 Results

3.1 Stage 1parameter sensitivity

3.1.1 Experiment 1: numerical scheme for bedload component calculations

Delft3D makes bed level change calculations at the centre of grid cells but bedload flux components are actually required at points between adjacent grid cells. Experiment 1 tested two numerical discretisation schemes, central (used for the baseline model) and upwind, to convert differential equations to algebraic equations that connect discrete nodes on the finite difference grid. Although central schemes are more accurate, since fluxes are less damped, they are also less stable than upwind schemes [cf *Deltares*, 2011; *Wright*, 2005].

Results (Figure 4) showed both schemes over-predicted volumes of erosion and deposition relative to that observed. Volumes of morphological change were approximately one-fifth lower for the central than for the upwind scheme, and closer to the observed volumes. Units of erosion and deposition were more spatially discrete for the central than the upwind scheme predictions. For example, scour was too deep and elongated for the upwind simulation in the vicinity of X on Figure 4a. The tendency for unrealistically deep scour along primary channels with the upwind scheme was also apparent in cross-section comparisons (Supplementary Figure 1). The histogram for the upwind scheme was characterised by a longer erosional tail attributed to over-deepening by scour. The distribution of bed elevation changes for the central scheme corresponded more closely to that observed, with similar minima and maxima of

279 elevations of scour and fill. There was a closer correspondence between observed and
280 predicted volumes of erosion than deposition.

281 **3.1.2 Experiment 2: hydraulics**

282 Figure 5 shows DoDs for the hydraulics sensitivity experiments. Sediment budget histograms
283 are shown in Supplementary Figure 2. Experiment 2a considered the importance of including
284 the effects of helical flow parameterisation, which causes the direction of bedload transport to
285 deviate from that predicted by depth-averaged flow and is important for point bar
286 development [*Dietrich and Smith*, 1983]. The simulation without helical flow parameterisation
287 under-predicted the tail of the erosion distribution. This was because the parameterisation of
288 helical flow corrected the direction of bed shear stress compared to that predicted by the
289 depth-averaged velocity vector, resulting in deeper scour at the outer bends of primary
290 channels and at confluences. Inspection of the DoDs also indicates that patterns of bar
291 development (e.g. in the vicinity of markers X and Y on Figure 5) were more natural for the
292 simulation with a parameterisation of helical flow. Thus, inclusion of helical flow
293 parameterisation resulted in more realistic confluence and outer bend scour.

294 Values of Nikuradse roughness length, k_s, horizontal eddy viscosity, v_H, and minimum flow
295 depth, d_{min}, for the baseline model were set based upon *Williams et al.'s* [2013] hydraulic
296 calibration for the same high-flow event that is being considered here (Table 1). Simulations for
297 k_s = 0.03 and 0.05 m (experiment 2b) resulted in erosion and deposition volumes decreasing by
298 4%, and increasing by 5% respectively compared to the baseline simulation. Since bed shear
299 stress is estimated by a quadratic friction law, changes in k_s of ± 0.01 m had only a relatively

300 minor impact on predicted depth and depth-averaged velocity, and hence bed shear stress and
301 morphological change.

302 Predicted volumes of change were relatively sensitive to an order of magnitude increase in
303 eddy viscosity (experiment 2c), with decreases in total erosion and deposition volumes of 8 and
304 12% respectively. Predictions for the simulation with higher v_H were associated with a tendency
305 for more longitudinally extensive units of erosion, such as that along the main channel in the
306 vicinity of Z (Figure 5). This resulted in longitudinally simplified channel geometry, with less
307 distinct pool and riffle morphology. These patterns were observed because higher v_H resulted in
308 lower transverse gradients of velocity and more widely distributed bed shear stress. Flows
309 remained competent but bed shear stresses were not as locally intense.

310 Experiment 2d considered uncertainty in discharge measurement [*Di Baldassarre and*
311 *Montanari*, 2009; *McMillan et al.*, 2010]. There were insufficient data to directly quantify
312 hydrograph uncertainty so a value of 15% was tested, based on *McMillan et al.'s* [2012]
313 benchmark for a similar site. Decreasing discharge by 15% decreased volumes of erosion by
314 13% and deposition by 15%; increasing discharge resulted in increases of 14 and 15% for
315 erosion and deposition volumes respectively. The approximately linear relationship between
316 changes in discharge and morphological change occurred because changes in discharge
317 resulted in the expansion or contraction of competent flow [*Ashmore and Sauks*, 2006] through
318 a network of channels across the braidplain that were characterised by similar dimensions.
319 Morphological predictions were relatively insensitive to varying the minimum flow depth from
320 0.10 to 0.05 m (experiment 2e) with predicted volumes of erosion and deposition varying by

1%. However, varying d_{min} did not change the threshold depth for sediment transport (*SedThr*) which was kept constant at 0.1 m. Thus, this change had only a minimal impact on predicted bed shear stresses along channels with competent flow.

3.1.3 Experiment 3: bed composition

Experiments were executed to investigate the sensitivity of the simulations to active and underlayer thickness (δ_a and δ_u respectively), initial bed composition, porosity and specific density, and sediment mixture (Table 2; Supplementary Figures 3 and 4). Experiment 3a considered δ_a and δ_u. Morphological predictions showed some sensitivity to active layer thickness, with decreases in δ_a resulting in less morphological change. Decreasing δ_u to 0.25 m curtailed erosion depths to 0.5 m because the base of the model was reached. Inspection of grain size distribution maps for the active layer for each simulation indicated that simulations with a thinner active layer developed a coarser active layer grain size distribution than those with a thicker active layer. This coarsening resulted in higher critical shear stress thresholds for bedload transport and resulted in less morphological change. The thickness of the minimum active layer simulated (0.1 m) is greater than the D_{84} grain size (37 ± 7 mm) of the surface layer.

At the start of each baseline simulation the active layer sediment size distribution was homogeneous across the model domain. In reality, grain size distributions would be spatially variable. To address this assumption, an initial simulation was run to redistribute multiple sediment fractions across the model domain whilst keeping the bed level fixed (Bed Composition Generation; BCG; *Van der Wegen et al.*, 2011). This was executed using the hydrograph from a precursor event, with a peak of 323 m^3s^{-1} (experiment 3b). Including BCG

342 resulted in decreases relative to the baseline of 4% erosion and 5% deposition, and a closer
343 match to the observed erosion histogram tail.

344 In addition to grain size distribution, sediment porosity and sediment density are needed to
345 calculate sediment transport and bed level change. A porosity of 0.4 is usually assumed
346 [*Mosselman*, 2005] but for mixed gravel sand sediment compositions, porosity is likely to be
347 lower. *Wu* and *Wang's* [2006] modification of established porosity formulas yielded a porosity
348 value of 0.26 for the Rees River's surface layer. This was within the range 0.02-0.36 measured
349 for gravel-bed rivers by *Milhous* [2001] and *Haschenburger and Roest* [2009]. For density, the
350 baseline simulation used 2,600 kg m^{-3} (quartz) but the mean density of schist is 2,732 kg m^{-3}
351 [*Tenzer et al.*, 2011]. Using physically realistic values for porosity and density (experiment 3c)
352 decreased volumes of erosion and deposition by c. 11 and 13% respectively. The predicted
353 change histogram for the revised sediment properties showed better correspondence than the
354 baseline predicted histogram, and the match was particularly good for the tail (<-0.25 m) of the
355 erosion distribution.

356 During model sensitivity testing, the baseline model used graded sediment, with the active and
357 bed layer initial conditions corresponding to the mean surface layer and subsurface
358 distributions respectively. Fractions in both layers were divided at one phi intervals, ranging
359 from very fine sand to medium boulder. The very fine sand fraction corresponded to the
360 smallest fraction of sediment grains that move as bedload by rolling, sliding or saltating [*Bridge*
361 *and Domenicco*, 2008]. A number of experiments were undertaken to test the sensitivity of

morphological predictions to the number of discrete sediment fractions simulated and the initial grain size distributions (experiment 3d).

The simulation that used a one phi grain size distribution from bulk sampling, for both active and underlayers, resulted in an increase in erosion and deposition relative to the baseline. The simulation with a uniform grain size resulted in deep scour and a relatively long erosion tail in the vertical change histogram. Using three grain classes also resulted in the over-prediction of morphological change because bed evolution and grain entrainment are overly simplified. Excluding the finest fraction (very fine sand) yielded a small decrease in morphological change. Testing the sensitivity of the predictions by adding one phi to the grain size distribution caused considerable under-prediction of larger magnitude volumetric changes. A final simulation considered the variation due to reducing the number of grain size fractions from one to two phi intervals (from 12 to 6 classes). This resulted in a *c.* 50% computational time saving, with only relatively small changes to the overall predicted volumetric change and negligible changes to the DoD. This contrasts to the model with 3 classes which resulted in greater time savings but unacceptable predictions.

3.1.4 Experiment 4: bedload transport and bed slope effects

Hicks and Gomez's [2005] recommendation of choosing bedload transport formulae on the basis of similarity with the river system upon which they were derived, and comparing the predictions of a number of formulae, was adopted for this paper. Model predictions were shown to be relatively sensitive to the choice of bedload transport formula (experiment 4a; Figure 6; Table 2; Supplementary Figure 5). The *Meyer-Peter and Müller* [MPM; 1948] bedload

383 transport formula, with no hiding and protrusion, over-predicted erosion. Incorporating the
384 *Egizarazaroff* [1965] hiding and protrusion correction reduced erosion and deposition volumes
385 by approximately one-quarter. A comparison between DoDs revealed variations in the
386 complexity of change. For example, morphological change in the vicinity of marker X
387 (Supplementary Figure 5) was dominated by deeper and more sinuous erosion using the
388 Egiazaroff correction compared to the simulation with no correction. Variations between the
389 *Wilcock and Crowe* [W&C; 2003] and the modified W&C formula [*Gaeuman et al.*, 2009] was
390 small. The higher volumetric change associated with the modified W&C formula, relative to the
391 W&C formula, is consistent with the coarsest fractions having greater susceptibility to
392 entrainment. The slightly lower volumetric change associated with the *Gaeuman et al.* [2009]
393 formula, relative to both W&C formulae, was due to the increase in reference shear stress.

394 The direction of bedload transport deviates from that predicted by depth-averaged flow due to
395 gravitational forces causing downward acceleration along longitudinal and transverse bed
396 slopes. Experiment 4b tested the parameterisation of these bed slope effects (see
397 supplementary information for formulae). The simulation with no bed slope effects resulted in
398 greater morphological change and deeper, more longitudinally elongated scour than the
399 simulation that included parameterisation of bed slope effects. The simulations that apply bed
400 slope formulations of *Bagnold* [1966] and *Ikeda* [1982], and *Talmon et al.* [1995] have similar
401 overall volumes of erosion and deposition, although the simulation that uses *Talmon et al.'s*
402 formulation was characterised by greater net erosion.

3.1.5 Experiment 5: bank erosion

Figure 7 shows five cross sections that compare observed and predicted bed levels for simulations with different bank erosion parametrization. Supplementary Figures 5 and 6 show DoDs and histograms. Table 2 lists sediment budgets. The simulation with no bank erosion was characterised by much deeper scour relative to the other simulations (e.g. A_1, D_3 and E_1 on Figure 7a). Moreover, channels did not erode laterally, resulting in relatively straight channels. Using the ThetSD bank erosion algorithm enabled the erosion of dry cells and thus mitigates the problem of channel overdeepening in simulations with no bank erosion (e.g. A_1, D_3 and E_1 on Figure 7a and Figure 7b). Comparison between the DoDs with no bank erosion and those with the ThetSD routine showed that for simulations with the ThetSD routine the largest channels (e.g. X on Supplementary Figure 6) evolved with greater sinuosity. However, the cross section plots (Figure 7b) indicate that there was a poor correspondence between the extent of lateral migration predicted by all three ThetSD parameterisations and that observed. For example, lateral channel shifting was in the wrong direction at marker A_1 and the predicted channel shape at marker E_1 is considerably different from that observed. From the perspective of the total sediment budget, estimates of erosion and deposition volumes were relatively insensitive to the parameterisation of ThetSD.

The repose routine was tested for a range of critical slopes varying from 0.1 to 0.3. The simulation with the shallowest critical slope, 0.1, had the tightest vertical change histogram distribution, with the tail of the erosion distribution closely matching the observed. As the critical slope was steepened, the sinuosity of evolving channels decreased and erosion as

deeper. Analysis of the total sediment budget therefore indicated that the repose algorithm performs better than the ThetSD algorithm. Inspection of the predicted cross sections (Figure 7c), however, indicates that disparities remained between the predicted and observed extents of lateral channel migration. At marker A_1 the repose routine with a critical slope of 0.1 produced a prediction that was closer to the observed channel geometry than the simulations with slopes of 0.2 and 0.3 but lateral migration on the true right of the channel was under-predicted to a similar magnitude as that observed for the ThetSD routine. At marker E_1 performance of the repose routine was similar to that predicted by the ThetSD routine.

3.1.6 Experiment 6: frequency of morphological calculations

Morphological change typically occurs on a longer timescale than corresponding changes in flow. Based on this, morphological models typically use a morphological time scale factor, *MorFac,* to speed up morphological changes to a rate where they influence flow dynamics. Existing applications of *MorFac* have focused upon scenarios with uniform sediment, and constant or cyclical flow. This has the advantage that the flow inputs can easily be compressed by reducing their duration (in the case of constant flow) or reducing the number of cycles (in the case of cyclic flow). Here, the objective was to test the application of *MorFac* to graded sediment and unsteady flow (experiment 6). In order to implement MorFac with unsteady flow the input flow hydrograph was compressed to reduce its duration in line with the applied scaling factor.

Results (Table 2 and Supplementary Figure 7) showed *MorFac* values of 2 and 5 caused some variation in total erosion and deposition volumes but the DoDs remained relatively consistent.

Applying MorFacs of 10 and 20 resulted in volumetric morphological change decreasing by approximately one-fifth and one-half respectively. The vertical change histogram for a MorFac of 10 showed a slight under-prediction of erosion. However, erosion and deposition volumes are 80 and 78% respectively of the baseline simulation so higher values of *MorFac*, in effect, damped the over-prediction of morphological change. The simulation with a *MorfFac* of 20 showed considerable under-prediction of both erosion and deposition.

3.2 Stage 2: calibration and assessment

Results from the sensitivity analysis were used for model tuning. A further set of simulations was executed that combined the best performing parameterisations from each sensitivity experiment. These simulations were executed for an additional 24 hours so that flows receded to 29 m^3s^{-1} at the end of the simulation (Figure 2). The calibrated model (Table 3; supplementary information movie 1) showed strong spatial coherence between units of observed and predicted morphological change (Figure 8). The tails of distribution of predicted and observed erosion and deposition volumes were similar. The predicted distribution was, however, more leptokurtic than the observed distribution. Predicted volumes of erosion and deposition were both greater than observed. The total erosion volume predicted (40,459 m^3) was within the observed 87% confidence interval (-37,024 ± 10,551 m^3) but the total deposition volume predicted (40,297 m^3) was greater than the observed 87% confidence interval (27,692 ± 9,842 m^3). A comparison between the observed and predicted post-event cross sections (Figure 8) shows that morphological change occured in similar parts of the braidplain. It also shows the

dimensions of observed and predicted channels were similar. In particular, the model did not over-predict the depth of scour.

Table 4 lists the results from metrics that compare the observed and predicted planimetric morphology of the study reach. Braiding intensity and confluence node density were predicted to be slightly lower after the high-flow event, indicated some network simplification. Metrics for the ratio between bar perimeter and bar area, and bar convex perimeter and bar perimeter were similar for both observations and predictions. The ratio between bar length and bar width was predicted to be lower than that observed.

4 Discussion

4.1 Parameter sensitivity analysis

An unsteady model of braided river morphodynamics has developed by starting with a sensitivity analysis, followed by model tuning and assessment. This section discusses findings from the sensitivity analysis, focusing upon important findings relating to bed composition, bedload transport, bank erosion, and the frequency of morphological calculations.

4.1.1 Bed composition

The sensitivity analysis demonstrated the importance of representing graded sediment in the model. *Nicholas* [2013c] suggested that his physics-based model of the Waimakariri had a tendency to generate cross sectional relief with a greater range than that observed because only a single grain size was represented in the model. This effect was confirmed by the single grain size model for the Rees, with erosion occurring to the bed of the underlayer at

485 confluences and towards the outer bank of primary channel bends. Multiple grain size fractions
486 are necessary to model armour layer formation; a ubiquitous feature of gravel-bed rivers [*Yager*
487 *and Schott*, 2013]. Results suggest two phi intervals are adequate for representing grain size
488 distribution, and representing the active layer with a slightly coarser grain size distribution is
489 appropriate.

490 Existing guidance suggests δ_a should equal D_{84} grain size for graded sediment or half the
491 bedform height for uniform sediment [*Mosselman*, 2012]. *Sloff and Mosselman* [2012],
492 however, found that it was necessary to use δ_a = 1 m for a graded sediment simulation of the
493 River Rhine's bifurcation, which was ten times thicker than half the dune height measured in
494 the field. Nicholas [2013c] used δ_a = 1 m for a uniform grain size simulation. Sensitivity analysis
495 results from the Rees modelling shows that morphological predictions are sensitive to δ_a due to
496 feedback associated with bed armouring. The calibrated model used δ_a = 0.25 m; a factor of 9
497 greater than subsurface D_{84}. The use of an initial BCG run to set a spatially-variable initial grain
498 size distribution in the active layer yielded smaller changes in bedload transport than observed
499 by *van der Wegen* [2011] for a simulation of San Pablo Bay, California. This is likely because the
500 San Pablo Bay model used a constant composition for the active and underlayers whereas for
501 the Rees model the initial active and underlayer sediment compositions were different (from
502 surface layer and bulk sediment sampling). The initial active layer of the Rees model is
503 therefore already better defined than that in the San Pablo Bay model.

4.1.2 Bedload transport and bank erosion

Transport of loosely consolidated sand and gravel bedload material in the Rees River is transport-limited. Entrainment is thus controlled by flow intensity, which is expressed in empirical bedload transport formulae in terms of shear stress on the river bed [*Warburton*, 2011]. The sensitivity testing of bedload transport formulae demonstrated the superior performance of formulas that included the effects of hiding and protrusion. The MPM formula, with no hiding and protrusion, over-predicted erosion as a consequence of the formula assuming equal mobility. The tendency for this bedload transport formula to cause deep scour has also been noted by *Kleinhans et al.* [2008]. Similar performance was obtained from the MPM formula with the addition of hiding and protrusion effects and the W&C formula, and associated variants, which were directly developed for predicting the transport of graded sediments. Comparative results, albeit using different non-uniform transport formulae, have been obtained from numerical model simulations of laboratory bends [*Fischer-Antze et al.*, 2009; *Feurich and Olsen*, 2011]. Overall, it is salient to note that, relative to the observed DoD, volumes from the Gaeuman et al. predictions over-estimated erosion by 26% and over-estimated deposition by 49%. It is notable that the magnitude of this difference is greater than the differences between the different transport formulae. However, this should be interpreted in the context of typical bedload transport equation performance, where predictions are estimated to be within a factor of two about two-thirds of the time [*Ackers and White*, 1973; *Gomez and Church*, 1989]. The total volumes of erosion and deposition, and the overall sediment balance of the monitored reach, are likely strongly influenced by sediment supply at the upstream boundary. All the modelling presented here used an equilibrium upstream

boundary condition for sediment and it is possible that by changing this a better fit with observed data could have been achieved. For example, by reducing sediment input it is likely that overall deposition volumes could have been reduced to better fit the observed data. The sediment balance may also be influenced by local transport-limited sediment transport in each grid cell. Accounting for a spatial lag between bed shear stress, and entrainment, transport and deposition of sediment may therefore be important. The Gaeuman et al. formula has the greatest physical basis for predicting sediment similar to the Rees. At the reach scale, the comparison of morphological change estimated using DoDs to those predicted by numerical modelling contributes to validating the Gaeuman et al. formula. Importantly, model predictions of low magnitude vertical change provide insight into morphodynamics that would be thresholded out from observations.

With respect to bank erosion, both the ThetSD and repose bank erosion routines were effective at preventing the channel over-deepening which prevailed without any bank erosion routine. Predictions were more sensitive to changes in the values of the repose angle than the proportion of sediment transferred from dry to wet cells using the ThetSD routine. This is because the repose angle is applied to neighbouring cells that are both wet-wet and wet-dry during each morphological timestep, whereas the ThetSD routine is only applied to neighbouring cells that are wet-dry. At low flows, when the bank is aerially exposed, bank erosion has been observed along the Rees River's braided channel network [*Rennie*, 2012; *Williams et al.*, 2015]. The exact dynamics of erosion of sharp banks at high flows, when the banks of bars are often inundated by shallow water, has not been directly monitored. It is likely, however, that inundated banks will continue to erode. The Repose routine is thus considered a

548 more physically plausible routine than the ThetSD routine but it does result in averaged bed
549 and bank slopes. The lateral migration rates that are predicted by both the Repose and ThetSD
550 routines do not match those observed. In some locations this could be due to propagation of
551 small errors in flow patterns, for example flow splits at diffluences, but it is also likely that both
552 bank erosion routines are overly simplified and miss key factors affecting erosion rate.

553 A fundamental improvement to numerical bank erosion schemes would be to make them
554 independent of grid resolution and orientation. Morphological modelling of braided rivers is
555 generally conducted at a resolution where bank height is similar or less than grid cell resolution,
556 meaning that bank slope is not well represented by the model grid. Bank height and bank toe
557 transport rate may thus be more suitable parameters than bank slope for use in any bank
558 erosion routine as they are likely to be less sensitive to cell resolution and orientation. Sub-grid
559 scale representation of banks (split cells) is one approach which solves resolution related issues
560 but it presents other difficulties including increased computational time and difficulty in
561 locating banks, especially during the drying and wetting of bar tops. In the Rees setting where
562 the braid banks are composed largely of cohesionless fine gravel and sand, incorporating the
563 effects or transient bank-toe protection by blocks of failed cohesive bank material (e.g. as
564 applied by *Ahasi et al.,* 2013) is unlikely to significantly influence the bank retreat process.

565 **4.1.3 Frequency of morphological calculations**

566 The results from the sensitivity analysis indicate that the predictions are more sensitive to
567 *MorFac* than has been reported elsewhere. For example, *Nicholas* [2013c] and *Kleinhans et al.*
568 [2008] reported that scaling factors of 100 and 200, respectively, have little discernible impact

569 on constant discharge or block-hydrographs. Here, the results from unsteady discharge
570 simulations indicate that a scaling factor of 20 results in significant under-prediction of
571 morphological change. The most likely explanation is that increasing MorFac causes the input
572 flow hydrograph to be compressed. The compressed hydrograph has steeper rising and falling
573 limbs. Flow is therefore less likely to attenuate over the length of the reach. A more physically
574 realistic approach to morphological acceleration might be to retain the same hydrograph and
575 hydraulic timestep but to make morphological calculations only on intermittent hydraulic
576 timesteps. This would not result in as big a timesaving as the currently implemented *MorFac*
577 approach available in Delft3D because it only reduces the effort involved in morphological
578 calculation rather than the effort in the hydraulic calculation as well. It would however have the
579 advantage that the hydraulics would not be compromised. This is particularly important for
580 simulation of the rapid variations in flow experienced during floods.

581 **4.2 Natural experiment data for model assessment**

582 The testing of the Delft3D model to determine the capability of the model to predict bed level
583 change for a single high-flow event is a step towards testing model predictions of natural river
584 morphodynamics over longer time-series. It is acknowledged that the morphological evolution
585 of braided rivers is sensitive to initial conditions [*Lane and Richards*, 1997], both in the field and
586 when modelling. Predictions of morphological change at the scale of individual high-flow events
587 are, however, likely to be characterised by less uncertainty than predictions of morphological
588 change forced by multiple high-flow events. A single high-flow event assessment of topographic
589 change is thus appropriate in this context.

There are only a limited number of natural experiment datasets that record the morphodynamics of braided rivers through a series of high-flow events. The Rees River DoDs are characterised by low vertical error compared to other natural experiment datasets, and are also supplemented by a continuous flow record. Following appropriate probabilistic thresholding, the DoDs have been shown to be suitable for morphodynamic model sensitivity testing. A remaining challenge for evaluating morphodynamic models with a DoD approach is to address the unknown flux of sediment in and out of the study reach from the upstream and downstream boundaries respectively. Whilst this flux can be measured by bedload sampling or the estimation of sediment step lengths, the uncertainty associated with fluxes into and out of the reach remains a primary source of error associated with using DoDs to assess morphological model predictions. Transport-limited upstream boundary conditions are assumed for the modelling reported here. Longer term simulation may, however, need to use an upstream boundary condition where bed level is not fixed and sediment input is not equal to the flow's local sediment transport capacity. Specification of non-equilibrium upstream boundary conditions will require consideration of sediment supply rate and composition, and how these vary across the width of the boundary and over time.

5 Conclusion

This study showed that a numerical model reproduced important features of bed level change in a braided river. Predictions of the location and total volume of erosion and deposition corresponded well to those observed. At the reach scale, morphological predictions validated the use of the Gaeuman et al. mixed grain size bedload transport formula; the difference

between predicted and observed volumes of erosion was less than the factor of two that typically characterises the accuracy of such predictions. Through a sensitivity analysis, observed and predicted DEMs of Difference were used to test model parameterisation. Observed and predicted planimetric metrics, such as braiding intensity and bar shape, were also used to gain further insight into the performance of the model. Whilst there are many ways to carry out a sensitivity analysis and calibration of a morphological model, the results and approach reported in this investigation are transferable to guide physics-based model applications to other rivers.

Results indicate that future model development efforts should be directed towards improving the realism of bank erosion processes in the model. In particular, the bank erosion scheme needs to be made independent of grid resolution and orientation. Such efforts need to be coupled with the application of suitable metrics to test whether lateral erosion rates are realistic and whether bedload transport pathways connect observed zones of erosion and deposition. There is also a need to test the sensitivity of the model to the upstream sediment boundary condition and to develop an appropriate framework for applying high morphological acceleration factors in unsteady flow simulations. The simulation of multiple high-flow events would provide further insight into model performance. Such modelling needs to be underpinned by the development of appropriate metrics that exploit the information in high resolution terrain data to enable the comparison of observed and predicted topography.

Acknowledgements

Becky Goodsell and Eric Scott are thanked for field assistance. Antony Smith assisted with figure production. The field campaign was funded by NERC Grant NE/G005427/1 and NERC

632 Geophysical Equipment Facility Loan 892. Richard Williams was funded by NERC Grant
633 NE/G005427/1 during fieldwork and by a British Hydrological Society Travel Grant whilst visiting
634 NIWA. Four reviewers provided constructive comments to improve this article. Data are
635 available by contacting the author directly (richard.williams@glasgow.ac.uk).

636 **Figure captions**

637 Figure 1 Morphological model domain and DoD. Aerial photos of study area acquired (a) before
638 and (b) after a 227 m^3s^{-1} high-flow event, showing extents of morphological model domain and
639 DoD. DEM acquired (c) before and (d) after the high-flow event. Note that the post-storm event
640 DEM has a smaller spatial extent than the pre-storm DEM. Comparisons between the observed
641 and predicted DoDs are thus restricted to the extent of the observed DoD. Techniques used to
642 survey topography for (e) pre- and (f) post-event DEMs. (g) Combined propagated error for
643 probabilistic DoD thresholding at 87% Confidence Interval. (h) DoD showing location of cross
644 sections used to compare observed and predicted bed levels.

645 Figure 2 Observed hydrograph, and predicted cumulative erosion and deposition, for simulation
646 of the 227 m^3s^{-1} high-flow event. Horizontal arrows also indicate hydrograph sections used for
647 sensitivity analysis (stage 1) and model tuning (stage 2).

648 Figure 3 Cumulative grain size distribution curves for (a) surface, (b) surface layer and (c)
649 subsurface sample data, and (d) comparison between the mean cumulative size distributions.

650 Figure 4 Numerical scheme sensitivity analysis (experiment 1). (a) DoDs. Letters identify areas
651 of interest that are discussed in the text. (b) Sediment budgets. The shaded area on the
652 histogram shows observed morphological change and the lines show model predictions.

653 Figure 5. DoDs for hydraulics sensitivity analysis (experiment 2). k_s is Nikuradse roughness
654 length. v_H is horizontal eddy viscosity. Q is discharge. d_{min} is minimum flow depth. Letters
655 identify areas of interest that are discussed in the text.

656 Figure 6 Sediment budgets for bedload transport sensitivity analysis (experiment 4a and b). The
657 shaded area on the histogram shows observed morphological change and the lines show model
658 predictions. MPM is Meyer-Peter and Müller. ξ is hiding and protrusion. BI is Bagnold and Ikeda.

659 Figure 7 Comparison between surveyed and predicted cross sections levels for bank erosion
660 sensitivity analysis (experiment 5): (A) No bank erosion. (B) ThetSD bank erosion routine. (C)
661 Repose bank erosion routine. Pre- and post-storm surveys are labelled DEM_1 and DEM_2
662 respectively. Cross sections are located across areas of pertinent morphological change, as
663 indicated on Figure 1h. Letters with numerical subscripts along each cross section are
664 positioned to aid comparison between (A), (B) and (C).

665 Figure 8 (A) Observed and predicted DoDs and sediment budget for calibrated model of 227
666 m^3s^{-1} event. (B) Comparison of observed and simulated cross sections (stage 2) of the 227 m^3s^{-1}
667 event. Pre- and post-storm surveys are labelled DEM_1 and DEM_2 respectively. Cross sections are
668 located across areas of pertinent morphological change, as indicated on Figure 1h.

669

Tables

Table 1 Model functions and parameters varied in sensitivity analysis experiments. n = number of simulations undertaken for experiment (including baseline).

Theme	Experiment	Function / parameter examined	Baseline model	n	Description of sensitivity runs
Numerical Scheme	1	Approach for bed level change calculations	Central scheme	2	Upwind scheme
Hydraulics	2a	Helical flow parameterization	Helical flow parameterisation off	2	Helical flow parameterisation on
	2b	Bed friction	k_s = 0.04 m	3	k_s = 0.03 and 0.05 m
	2c	Horizontal eddy viscosity	ν_H = 0.1 m^2s^{-1}	2	ν_H = 1 m^2s^{-1}
	2d	Discharge	Invincible gauge hydrograph	3	Invincible gauge hydrograph ±15%
	2e	Minimum flow depth	d_{min} = 0.10 m	2	d_{min} = 0.05 m
Bed composition	3a	Active and under layer thickness	δ_a = 0.25, δ_u = 2 m	6	δ_a = 0.10, 0.50 with δ_u = 2.00 m with δ_a = 0.05, 0.10, 0.25 m and δ_u = 0.25 m
	3b	Initial bed composition generation (BCG)	No BCG	2	Initial bed composition generation from prior high-flow event
	3c	Porosity and specific density	ϕ = 0.4, ρ = 2600 kgm^{-3}	2	ϕ = 0.26, ρ = 2732 kgm^{-3}
	3d	Sediment mixture	One φ intervals based on surface layer and bulk sampling	7	One φ intervals based on bulk sampling Uniform grain size based on D_{50} of bulk sampling Division of intervals into sand, gravel and cobble based on surface layer and bulk sampling Finer: one φ intervals based on surface layer and bulk sampling with exclusion of very fine sand Coarser: all fractions increased by one φ, based on surface layer and bulk sampling Two φ intervals based on surface layer and bulk sampling
Bedload transport	4a	Transport equation	Gaeuman et al.	8	MPM with no ξ MPM with Egiazaroff ξ Wilcock and Crowe Modified Wilcock and Crowe
	4b	Bed slope effects	Bagnold and Ikeda	3	α_{bs} = 0 Talmon et al.
Bank erosion	5	Repose and simple models	Repose = 0.2	7	No bank erosion ThetSD = 0.25, 0.50, 0.75 Repose = 0.1, 0.3
Calculation frequency	6b	Morphological factor	MorFac = 1	5	MorFac = 2, 5, 10, 20

Table 2 Predicted volumes of morphological change for bed composition (Experiment 3), bedload transport (Experiment 4), bank erosion (Experiment 5), frequency of calculation (Experiment 6) and spatial resolution (Experiment 7) sensitivity tests. The parameterization column describes how parameters were varied from those defined for the baseline model (as listed in Table 1). δ_a is active layer. δ_u is under layer. BCG is bed composition generation. Φ is porosity. ρ is density. a is active layer. u is under layer. ϕ is grain size interval (i.e. 1 ϕ refers to a simulations with multiple grain sizes with 1 ϕ size divisions; 2 ϕ refers to a simulations with multiple grain sizes with 2 ϕ size divisions). BLT is bedload transport. MPM is Meyer-Peter and Müller. ξ is hiding and protrusion.

Experiment	Parameterization	Erosion, m^3 (% change from baseline)	Deposition, m^3 (% change from baseline)	Net, m^3
Observed	Not applicable	-37,024 ± 10,551	27,692 ± 9,842	-9,331 ± 14,429
Baseline	δ_a = 0.25 m, δ_u = 2.00 m No initial BCG ϕ = 0.40, ρ = 2,600 kgm^{-3} 1ϕ fractions. a: surface layer, b: bulk BLT: Gaeuman *et al.* Bed slope: Bagnold and Ikeda (BI) Repose = 0.2 MorFac = 1 Δx = 3 m	-41,770 (%)	41,351 (%)	-419
3a	δ_a = 0.10 m, δ_u = 2.00 m	-40,233 (-4%)	39,308 (-5%)	-926
3a	δ_a = 0.50 m, δ_u = 2.00 m	-43,444 (4%)	43,090 (4%)	-354
3a	δ_a = 0.10 m, δ_u = 0.25 m	-34,105 (-18%)	34,899 (-16%)	794
3b	Initial BCG	-40,233 (-4%)	39,308 (-5%)	-926
3c	ϕ = 0.26, ρ = 2732 kgm^{-3}	-36,973 (-11%)	36,138 (-13%)	-835
3d	1 φ intervals. a: bulk, b: bulk	-43,072 (3%)	42,713 (3%)	-360
3d	Uniform grain size from D_{50} bulk	-56,688 (36%)	37,314 (-10%)	-19,374
3d	Three fractions. a: surface layer, b: bulk	-51,859 (24%)	53,182 (29%)	1,323
3d	Finer (no very fine sand). a: adjusted surface layer, b: adjusted bulk.	-40,933 (-2%)	40,142 (-3%)	-791
3d	Coarser (all fractions increased by 1 φ). a: adjusted surface layer, b: adjusted bulk	-25,112 (-40%)	23,519 (-43%)	-1,593
3d	2 φ intervals. a: surface layer, b: bulk	-43,315 (4%)	42,925 (4%)	-390
4a	BLT: MPM,no ξ. Bed slope: BI	-48,735 (17%)	50,095 (21%)	1,360
4a	BLT: MPM, Egiazaroff ξ. Bed slope: BI	-39,343 (-6%)	38,528 (-7%)	-815
4a	BLT: Wilcock and Crowe. Bed slope: BI	-42,064 (1%)	42,174 (2%)	110
4a	BLT: Modified Wilcock and Crowe. Bed slope: BI	-42,722 (2%)	42,973 (4%)	250
4b	BLT: Gaeuman *et al.* Bed slope: no bed slope effect	-49,931 (20%)	49,450 (20%)	-481
4b	BLT: Gaeuman *et al*. Bed slope: Talmon *et al.*	-42,717 (2%)	41,898 (1%)	-819
5	No bank erosion	-41,891 (0%)	40,449 (-2%)	-1,443
5	ThetSD = 0.25	-42,250 (1%)	40,789 (-1%)	-1,462
5	ThetSD = 0.50	-42,473 (2%)	40,841 (-1%)	-1,633
5	ThetSD = 0.75	-42,856 (3%)	41,152 (0%)	-1,704
5	Repose = 0.1	-39,936 (-4%)	41,489 (0%)	1,553
5	Repose = 0.3	-42,494 (2%)	41,388 (0%)	-1,106
6	MorFac = 2	-40,891 (-2%)	41,440 (0%)	549
6	MorFac = 5	-41,631 (0%)	40,580 (-2%)	-1,050
6	MorFac = 10	-33,545 (-20%)	32,241 (-22%)	-1,304
6	MorFac = 20	-20,908 (-50%)	20,114 (-51%)	-794

695

696

697

698

699 Table 3 Model functions and values of parameters used in calibrated model of 227 m^3s^{-1} event.

Function / parameter	Value
Numerical scheme for bed level change calculations	Central
Helical flow parameterisation	On
Bed friction	k_s = 0.05 m
Horizontal eddy viscosity	v_H = 0.1 m^2s^{-1}
Discharge	Invincible gauge hydrograph
Minimum flow depth	d_{min} = 0.05 m
Threshold depth for sediment calculations	*SedThr* = 0.1 m
Active layer thickness	δ_a = 0.25 m
Under layer thickness	δ_u = 2 m
Initial bed composition generation	Generated from precursor storm event
Porosity	Φ = 0.26
Specific density	ρ = 2732 kgm^{-3}
Sediment mixture (active layer)	One φ intervals based on surface layer sampling
Sediment mixture (under layer)	One φ intervals based on bulk sampling
Bed-material transport equation	Gaeuman et al. [2009]
Bed slope effects	Talmon et al. [1995]
Bank erosion model	*Repose* = 0.2
Hydraulic timestep	Δt = 0.6 s
Morphological factor	*MorFac* = 5
Grid resolution	Δx = 3 m

700

701

702 Table 4 Metrics used to assess calibrated model performance. Values were calculated from running a 100 m^3s^{-1}

703 steady state hydrodynamic simulation across observed and predicted DEMs.

Metric		Observed	Predicted
Braiding intensity		6.8	6.4
Confluence node density, nodes km^{-2}		91	83
Least squares regression coefficient of determination, R^2, for relationship between:	Bar perimeter and bar area	0.986	0.985
	Bar length and bar width	0.903	0.881
	Bar convex perimeter	0.999	0.999

704

705

706 **References**

707 Ackers, P., and W. R. White (1973), Sediment transport: New approach and analysis, *Journal of*
708 *the Hydraulics Division - ASCE*, *99*, 2041-2060.

709 Asahi, K., Shimizu, Y., Nelson, J., Parker, G. (2013), Numerical simulation of river meandering
710 with self-evolving banks, *Journal of Geophysical Research: Earth Surface*, 118: 2208–2229,
711 doi:10.1002/jgrf.20150.

712 Ashmore, P. E., and M. A. Church (1998), Sediment transport and river morphology: a paradigm
713 for study, in *Gravel Bed Rivers in the Environment*, edited by P. C. Klingeman, R. L.
714 Beschta, B. D. Komar and J. B. Bradley, pp. 115-139, Water Resources Publications,
715 Oregon.

716 Ashmore, P. E., and E. Sauks (2006), Prediction of discharge from water surface width in a
717 braided river with implications for at-a-station hydraulic geometry, *Water Resources*
718 *Research*, *42*(3), W03406.

719 Ashworth, P. J., and R. I. Ferguson (1986), Interrelationships of channel processes, changes and
720 sediments in a proglacial braided river, *Geografiska Annaler. Series A, Physical Geography*,
721 *68*(4), 361-371.

722 Bagnold, R. A. (1966), An approach to the sediment transport problem from general
723 physics*Rep.*, 42 pp, Washington, DC.

724 Blott, S. J., and K. Pye (2001), GRADISTAT: a grain size distribution and statistics package for the
725 analysis of unconsolidated sediments, *Earth Surface Processes and Landforms*, *26*(11),
726 1237-1248.

727 Brasington, J. (2010), From Grain to Floodplain: Hyperscale Models of Braided Rivers, *Journal of*
728 *Hydraulic Research*, *48*(4), 52-53.
729 Brasington, J., J. Langham, and B. Rumsby (2003), Methodological sensitivity of morphometric
730 estimates of coarse fluvial sediment transport, *Geomorphology*, *53*(3-4), 299-316.
731 Brasington, J., D. Vericat, and I. Rychkov (2012), Modelling river bed morphology, roughness
732 and surface sedimentology using high resolution terrestrial laser scanning, *Water*
733 *Resources Research*, *48*, W11519.
734 Bridge, J. S., and R. Domenicco (2008), *Earth surface processes, landforms and sediment*
735 *deposits*, Cambridge University Press, Cambridge.
736 Carbonneau, P. E., and H. Piégay (2012), *Fluvial remote sensing for science and management*,
737 434 pp., Wiley-Blackwell, Oxford.
738 Carrivick, J. L., M. Geilhausen, J. Warburton, N. E. Dickson, S. J. Carver, A. J. Evans, and L. E.
739 Brown (2012), Contemporary geomorphological activity throughout the proglacial area of
740 an alpine catchment, *Geomorphology*.
741 Church, M., and R. I. Ferguson (2015), Morphodynamics: Rivers beyond steady state, *Water*
742 *Resources Research*, *51*(4), 1883-1897.
743 Church, M., D. G. McLean, and J. F. Walcott (1987), River bed gravels: sampling and analysis, in
744 *Sediment Transport in Gravel-Bed Rivers*, edited by C. R. Thorne, J. C. Bathurst and R. D.
745 Hey, pp. 43-88, John Wiley and Sons, Chichester.
746 Cook, S. J., D. J. Quincey, and J. Brasington (2014), Geomorphology of the Rees Valley, Otago,
747 New Zealand, *Journal of Maps*, *10*(1), 136-150.

748 Crosato, A., and M. S. Saleh (2011), Numerical study on the effects of floodplain vegetation on
749 river planform style, *Earth Surface Processes and Landforms*, *36*(6), 711-720.
750 Deltares (2011), Delft3D-FLOW, *a documentation report Rep.*, 688 pp, Deltares, Delft, The
751 Netherlands.
752 DeVries, P. (2002), Bedload Layer Thickness and Disturbance Depth in Gravel Bed Streams,
753 *Journal of Hydraulic Engineering*, *128*(11), 983-991.
754 Di Baldassarre, G., and A. Montanari (2009), Uncertainty in river discharge observations: a
755 quantitative analysis, *Hydrol. Earth Syst. Sci.*, *13*(6), 913-921.
756 Dietrich, W. E., and J. D. Smith (1983), Influence of the point bar on flow through curved
757 channels, *Water Resources Research*, *19*(5), 1173-1192.
758 Egiazaroff, I. V. (1965), Calculation of non-uniform sediment concentrations, *Journal of*
759 *Hydraulic Engineering*, *91*(4), 225-248.
760 Ferguson, R. I. (1993), Understanding braiding processes in gravel-bed rivers: progress and
761 unresolved problems, in *Braided Rivers*, edited by J. L. Best and C. S. Bristow, pp. 73-87,
762 Geological Society, London.
763 Ferguson, R. I. (2007), Gravel-bed rivers at the reach scale, in *Gravel Bed Rivers VI: From Process*
764 *Understanding to River Restoration*, edited by H. M. Habersack, H. Piégay and M. Rinaldi,
765 pp. 33-53, Elsevier.
766 Feurich, R., and N. Olsen (2011), Three-Dimensional Modeling of Nonuniform Sediment
767 Transport in an S-Shaped Channel, *Journal of Hydraulic Engineering*, *137*(4), 493-495.

768 Fischer-Antze, T., N. R. B. Olsen, and D. Gutknecht (2008), Three-dimensional CFD modeling of
769 morphological bed changes in the Danube River, *Water Resources Research*, *44*(9),
770 W09422.
771 Fischer-Antze, T., N. Rüther, N. R. B. Olsen, and D. Gutknecht (2009), Three-dimensional (3D)
772 modeling of non-uniform sediment transport in a channel bend with unsteady flow,
773 *Journal of Hydraulic Research*, *47*(5), 670-675.
774 Gaeuman, D., E. D. Andrews, A. Krause, and W. Smith (2009), Predicting fractional bed load
775 transport rates: Application of the Wilcock-Crowe equations to a regulated gravel bed
776 river, *Water Resources Research*, *45*(6), W06409.
777 Gomez, B., and M. Church (1989), An assessment of bed load sediment transport formulae for
778 gravel bed rivers, *Water Resources Research*, *25*(6), 1161-1186.
779 Haschenburger, J. K., and P. Roest (2009), Substrate indices as indicators of interstitial pore
780 space in gravel-bed channels, *River Research and Applications*, *25*(1), 98-105.
781 Hicks, D. M., and B. Gomez (2005), Sediment Transport, in *Tools in Fluvial Geomorphology*,
782 edited by G. M. Kondolf and H. Piegay, pp. 425-461, Wiley, Chichester, England.
783 Hicks, D. M., U. Shankar, M. J. Duncan, M. Rebuffé, and J. Aberle (2006), Use of Remote-Sensing
784 with Two-Dimensional Hydrodynamic Models to Assess Impacts of Hydro-Operations on a
785 Large, Braided, Gravel-Bed River: Waitaki River, New Zealand, in *Braided Rivers: Process,*
786 *Deposits, Ecology and Management*, edited by G. H. Sambrook Smith, J. L. Best, C. S.
787 Bristow and G. E. Petts, pp. 311-326, Blackwell Publishing Ltd., Oxford.
788 Hirano, M. (1971), River bed degradation with armouring, *Transaction of the Japan Society of*
789 *Civil Engineering*, *195*(11), 55-65.

790 Howard, A. D., M. E. Keetch, and C. L. Vincent (1970), Topological and geometrical properties of
791 braided streams, *Water Resources Research*, 6, 1674-1688.
792 Ikeda, S. (1982), Incipient motion of sand particles on side slopes, *Journal of Hydraulics Division,*
793 *ASCE*, *108*(1), 95-114.
794 Jang, C. L., and Y. Shimizu (2005), Numerical Simulation of Relatively Wide, Shallow Channels
795 with Erodible Banks, *Journal of Hydraulic Engineering*, *131*(7), 565-575.
796 Javernick, L., J. Brasington, and B. Caruso (2014), Modelling the topography of shallow braided
797 rivers using Structure-from-Motion photogrammetry, *Geomorphology*, *213*, 166-182.
798 Javernick, L., D. M. Hicks, R. Measures, B. Caruso, and J. Brasington (2016), Numerical Modelling
799 of Braided Rivers with Structure-from-Motion-Derived Terrain Models, *River Research and*
800 *Applications*, 32, 1071-1081.
801 Jowett, I. G., and M. J. Duncan (2012), Effectiveness of 1D and 2D hydraulic models for instream
802 habitat analysis in a braided river, *Ecological Engineering*, *48*, 92-100.
803 Karmaker, T., and S. Dutta (2016), Prediction of Short-Term Morphological Change in Large
804 Braided River Using 2D Numerical Model, *Journal of Hydraulic Engineering*, doi:
805 10.1061/(ASCE)HY.1943-7900.0001167.
806 Kelly, S. (2006), Scaling and Hierarchy in Braided Rivers and their Deposits: Examples and
807 Implications for Reservoir Modelling, in *Braided Rivers*, edited by G. H. Sambrook Smith, J.
808 L. Best, C. S. Bristow and G. E. Petts, pp. 75-106, Blackwell Publishing Ltd., Oxford.
809 Kleinhans, M. G. (2010), Sorting out river channel patterns, *Progress in Physical Geography*,
810 *34*(3), 287-326.

811 Kleinhans, M. G., H. R. A. Jagers, E. Mosselman, and C. J. Sloff (2008), Bifurcation dynamics and
812 avulsion duration in meandering rivers by one-dimensional and three-dimensional
813 models, *Water Resources Research*, *44*(8), W08454.
814 Klingeman, P. C., and W. W. Emmett (1982), Gravel bedload transport processes, in *Gravel Bed*
815 *Rivers*, edited by R. D. Hey, J. C. Bathurst and C. R. Thorne, pp. 141-179, Wiley, London.
816 Klingeman, P. C., C. J. Chaquette, and S. B. Hammond (1979), Bed material characteristics near
817 Oak Creek Sediment Transport Research Facilities, 1978-1979*Rep.*, Water Resrouces
818 Research Institute, Oregon State University, Corvallis, Oregon.
819 Knight, D. W. (2013), River hydraulics – a view from midstream, *Journal of Hydraulic Research*,
820 *51*(1), 2-18.
821 Lallias-Tacon, S., F. Liébault, and H. Piégay (2014), Step by step error assessment in braided
822 river sediment budget using airborne LiDAR data, *Geomorphology*, *214*, 307-323.
823 Lane, S. N. (2000), The Measurement of River Channel Morphology Using Digital
824 Photogrammetry, *The Photogrammetric Record*, *16*(96), 937-961.
825 Lane, S. N., and K. S. Richards (1997), Linking river channel form and process: Time, space and
826 causality revisited, *Earth Surface Processes and Landforms*, *22*(3), 249-260.
827 Lane, S. N., and J. H. Chandler (2003), Editorial: the generation of high quality topographic data
828 for hydrology and geomorphology: new data sources, new applications and new
829 problems, *Earth Surface Processes and Landforms*, *28*(3), 229-230.
830 Lane, S. N., R. M. Westaway, and D. M. Hicks (2003), Estimation of erosion and deposition
831 volumes in a large, gravel-bed, braided river using synoptic remote sensing, *Earth Surface*
832 *Processes and Landforms*, *28*(3), 249-271.

833 Lane, S. N., P. E. Widdison, R. E. Thomas, P. J. Ashworth, J. L. Best, I. A. Lunt, G. H. S. Smith, and
834 C. J. Simpson (2010), Quantification of braided river channel change using archival digital
835 image analysis, *Earth Surface Processes and Landforms*, *35*(8), 971-985.
836 Leopold, L. B. (1992), Sediment size that determines channel geometry., in *Dynamics of Gravel-*
837 *Bed Rivers*, edited by P. Billi, R. D. Hey, C. R. Thorne and P. Tacconi, pp. 297-311, Wiley,
838 Chichester.
839 Lesser, G. R., J. A. Roelvink, J. A. T. M. van Kester, and G. S. Stelling (2004), Development and
840 validation of a three-dimensional morphological model, *Coastal Engineering*, *51*(8–9),
841 883-915.
842 Lotsari, E., D. Wainwright, G. D. Corner, P. Alho, and J. Käyhkö (2013), Surveyed and modelled
843 one-year morphodynamics in the braided lower Tana River, *Hydrological Processes*, n/a-
844 n/a.
845 McMillan, H. K., T. Krueger, and J. Freer (2012), Benchmarking observational uncertainties for
846 hydrology: rainfall, river discharge and water quality, *Hydrological Processes*, *26*(26),
847 4078-4111.
848 McMillan, H. K., J. Freer, F. Pappenberger, T. Krueger, and M. Clark (2010), Impacts of uncertain
849 river flow data on rainfall-runoff model calibration and discharge predictions,
850 *Hydrological Processes*, *24*(10), 1270-1284.
851 Meyer-Peter, E., and R. Müller (1948), Formulas for bedload transport, paper presented at
852 Proceedings of the 2nd meeting of the International Association for Hydraulic Research,
853 International Association of Hydraulic Engineering and Research, Madrid, Stockholm,
854 Sweden.

855 Milan, D. J., G. L. Heritage, and D. Hetherington (2007), Application of a 3D laser scanner in the
856 assessment of erosion and deposition volumes and channel change in a proglacial river,
857 *Earth Surface Processes and Landforms*, *32*(11), 1657-1674.
858 Milhous, R. T. (2001), Specific weight and median size of the bed material of gravel and cobble
859 bed rivers., in *Proceedings of the Seventh Federal Interagency Sedimentation Conference*,
860 edited, Reno, Nevada.
861 Montgomery, D. R., and J. M. Buffington (1997), Channel-reach morphology in mountain
862 drainage basins, *Geological Society of America Bulletin*, *109*(5), 596-611.
863 Moretto, J., E. Rigon, L. Mao, F. Delai, L. Picco, and M. A. Lenzi (2014), Short-term geomorphic
864 analysis in a disturbed fluvial environment by fusion of LiDAR, colour bathymetry and
865 dGPS surveys, *CATENA*, *122*(0), 180-195.
866 Mosselman, E. (2005), Basic Equations for Sediment Transport in CFD for Fluvial
867 Morphodynamics, in *Computational Fluid Dynamics*, edited, pp. 71-89, John Wiley & Sons,
868 Ltd.
869 Mosselman, E. (2012), Modelling Sediment Transport and Morphodynamics of Gravel-Bed
870 Rivers, in *Gravel-Bed Rivers*, edited, pp. 101-115, John Wiley & Sons, Ltd.
871 Murray, A. B., and C. Paola (1994), A Cellular-Model of Braided Rivers, *Nature*, *371*(6492), 54-
872 57.
873 Murray, A. B., and C. Paola (2003), Modelling the effect of vegetation on channel pattern in
874 bedload rivers, *Earth Surface Processes and Landforms*, *28*(2), 131-143.
875 Nicholas, A. P. (2013a), Morphodynamic diversity of the world's largest rivers, *Geology*, *41*(4),
876 475-478.

877 Nicholas, A. P. (2013b), Morphodynamic Modeling of Rivers and Floodplains, in *Fluvial*
878 *Geomorphology, Treatise on Geomorphology*, edited by E. Wohl, pp. 160-179, Academic
879 Press, San Diego.
880 Nicholas, A. P. (2013c), Modelling the continuum of river channel patterns, *Earth Surface*
881 *Processes and Landforms*, *38*(10), 1187-1196.
882 Nicholas, A. P., S. D. Sandbach, P. J. Ashworth, M. L. Amsler, J. L. Best, R. J. Hardy, S. N. Lane, O.
883 Orfeo, D. R. Parsons, A. J. H. Reesink, G. H. Sambrook Smith, and R. N. Szupiany (2012),
884 Modelling hydrodynamics in the Rio Paraná, Argentina: An evaluation and inter-
885 comparison of reduced-complexity and physics based models applied to a large sand-bed
886 river, Geomorphology, 169-170, 192-211.Passalacqua, P., P. Belmont, D. M. Staley, J. D.
887 Simley, J. R. Arrowsmith, C. A. Bode, C. Crosby, S. B. DeLong, N. F. Glenn, S. A. Kelly, D.
888 Lague, H. Sangireddy, K. Schaffrath, D. G. Tarboton, T. Wasklewicz, and J. M. Wheaton
889 (2015), Analyzing high resolution topography for advancing the understanding of mass
890 and energy transfer through landscapes: A review, *Earth-Science Reviews*, *148*(0), 174-
891 193.
892 Rennie, C. D. (2012), Mapping Water and Sediment Flux Distributions in Gravel-Bed Rivers Using
893 ADCPs, in *Gravel-Bed Rivers*, edited, pp. 342-350, John Wiley & Sons, Ltd.
894 Schuurman, F., and M. G. Kleinhans (2015), Bar dynamics and bifurcation evolution in a
895 modelled braided sand-bed river, *Earth Surface Processes and Landforms*, *40*(10), 1318-
896 1333.

897 Schuurman, F., W. A. Marra, and M. G. Kleinhans (2013), Physics-based modeling of large
898 braided sand-bed rivers: bar pattern formation, dynamics and sensitivity, *Journal of*
899 *Geophysical Research: Earth Surface*, *118*(4), 2509-2527.
900 Sloff, K., and E. Mosselman (2012), Bifurcation modelling in a meandering gravel–sand bed
901 river, *Earth Surface Processes and Landforms*, *37*(14), 1556-1566.
902 Stelling, G. S., and J. J. Leendertse (1992), Approximation of convective processes by cyclic AOI
903 methods, in *Estuarine and coastal modeling*, edited by M. L. Spaulding, K. Bedford and A.
904 Blumberg, pp. 771-782, ASCE, Tampa.
905 Sun, J., B. Lin, and H. Yang (2015), Development and application of a braided river model with
906 non-uniform sediment transport, *Advances in Water Resources*, *81*, 62-74.
907 Talmon, A. M., N. Struiksma, and M. C. L. M. Van Mierlo (1995), Laboratory measurements of
908 the direction of sediment transport on transverse alluvial-bed slopes, *Journal of Hydraulic*
909 *Research*, *33*(4), 495-517.
910 Tarolli, P. (2014), High-resolution topography for understanding Earth surface processes:
911 Opportunities and challenges, *Geomorphology*, *216*, 295-312.
912 Tenzer, R., P. Sirguey, M. Rattenbury, and J. Nicolson (2011), A digital rock density map of New
913 Zealand, *Computers and Geosciences*, *37*(8), 1181-1191.
914 Tucker, G. E. (2009), Natural experiments in landscape evolution, *Earth Surface Processes and*
915 *Landforms*, *34*(10), 1450-1460.
916 van der Wegen, M., and J. A. Roelvink (2008), Long-term morphodynamic evolution of a tidal
917 embayment using a two-dimensional, process-based model, *J. Geophys. Res.*, *113*(C3),
918 C03016.

van der Wegen, M., Z. B. Wang, H. H. G. Savenije, and J. A. Roelvink (2008), Long-term morphodynamic evolution and energy dissipation in a coastal plain, tidal embayment, *J. Geophys. Res.*, *113*(F3), F03001.

van der Wegen, M., A. Dastgheib, B. Jaffe, and D. Roelvink (2011), Bed composition generation for morphodynamic modeling: case study of San Pablo Bay in California, USA, *Ocean Dynamics*, *61*(2), 173-186.

van der Werff, H. M. A., and F. D. van der Meer (2008), Shape-based classification of spectrally identical objects, *ISPRS Journal of Photogrammetry and Remote Sensing*, 63(2), 251-258.

Warburton, J. (2011), Sediment transport and deposition, in *The SAGE Handbook of Geomorphology*, edited by K. J. Gregory and A. S. Goudie, pp. 326-342, SAGE, London.

Westaway, R. M., S. N. Lane, and D. M. Hicks (2003), Remote survey of large-scale braided, gravel-bed rivers using digital photogrammetry and image analysis, *International Journal of Remote Sensing*, *24*(4), 795-815.

Wheaton, J. M., J. Brasington, S. E. Darby, and D. A. Sear (2010), Accounting for uncertainty in DEMs from repeat topographic surveys: improved sediment budgets, *Earth Surface Processes and Landforms*, *35*(2), 136-156.

Wilcock, P. R., and J. C. Crowe (2003), Surface-based transport model for mixed-size sediment, *Journal of Hydraulic Engineering-Asce*, *129*(2), 120-128.

Wilcock, P. R., S. T. Kenworthy, and J. C. Crowe (2001), Experimental study of the transport of mixed sand and gravel, *Water Resources Research*, *37*(12), 3349-3358.

939 Wilcock, P. R., J. Pitlick, and Y. Cui (2009), Sediment transport primer: estimating bed-material
940 transport in gravel-bed rivers*Rep.*, 78 pp, United States Department of Agriculture, Forest
941 Service, Rocky Mountain Research Station, Fort Collins, CO.
942 Williams, R. D. (2014), Two-dimensional numerical modelling of natural braided river
943 morphodynamics, 492 pp, University of Aberystwyth, Aberystwyth.
944 Williams, R. D., J. Brasington, and D. M. Hicks (2016), Numerical modelling of braided river
945 morphodynamics: review and future challenges, *Geography Compass*.
946 Williams, R. D., J. Brasington, D. Vericat, and D. M. Hicks (2014), Hyperscale terrain modelling of
947 braided rivers: fusing mobile terrestrial laser scanning and optical bathymetric mapping,
948 *Earth Surface Processes and Landforms*, *39*(2), 167-183.
949 Williams, R. D., C. R. Rennie, J. Brasington, D. M. Hicks, and D. Vericat (2015), Within-event
950 spatially distributed bed material transport: linking apparent bedload velocity to
951 morphological change, *Journal of Geophysical Research: Earth Surface*, *120*(3), 604-622.
952 Williams, R. D., J. Brasington, D. Vericat, D. M. Hicks, F. Labrosse, and M. Neal (2011),
953 Monitoring braided river change using terrestrial laser scanning and optical bathymetric
954 mapping, in *Geomorphological mapping: methods and applications*, edited by M. Smith,
955 P. Paron and J. Griffiths, pp. 507-532, Elsevier, Amsterdam.
956 Williams, R. D., J. Brasington, M. Hicks, R. Measures, C. D. Rennie, and D. Vericat (2013),
957 Hydraulic validation of two-dimensional simulations of braided river flow with spatially
958 continuous aDcp data, *Water Resources Research*, *49*(9), 5183-5205.
959 Wolman, M. G. (1954), A method of sampling coarse bed material, *Transactions of the*
960 *American Geophysical Union*, *35*, 951-956.

961 Wright, N. G. (2005), Introduction to Numerical Methods for Fluid Flow, in *Computational Fluid*
962 *Dynamics*, edited by P. Bates, S. Lane and R. Ferguson, pp. 147-168, John Wiley & Sons,
963 Ltd, Chichester.
964 Wu, W. (2008), *Computational river dynamics*, 494 pp., Taylor & Francis, London.
965 Wu, W., and S. Wang (2006), Formulas for Sediment Porosity and Settling Velocity, *Journal of*
966 *Hydraulic Engineering*, *132*(8), 858-862.
967 Xia, J. Q., Z. B. Wang, Y. P. Wang, and X. Yu (2013), Comparison of Morphodynamic Models for
968 the Lower Yellow River, *Journal of the American Water Resources Association*, *49*(1), 114-
969 131.
970 Yager, E. M., and H. E. Schott (2013), The Initiation of Sediment Motion and Formation of Armor
971 Layers, in *Fluvial Geomorphology, Treatise on Geomorphology*, edited by E. Wohl, pp. 87-
972 102, Academic Press, San Diego.
973 Yang, H., B. Lin, and J. Zhou (2015), Physics-based numerical modelling of large braided rivers
974 dominated by suspended sediment, *Hydrological Processes*, *29*(8), 1925-1941.

975 Ziliani, L., N. Surian, T. J. Coulthard, and S. Tarantola (2013), Reduced-complexity modeling of
976 braided rivers: assessing model performance by sensitivity analysis, calibration and
977 validation, *Journal of Geophysical Research: Earth Surface*, 118(4), 2243-2262, doi:
978 10.1002/jgrf.20154.

Figure 1. Figure

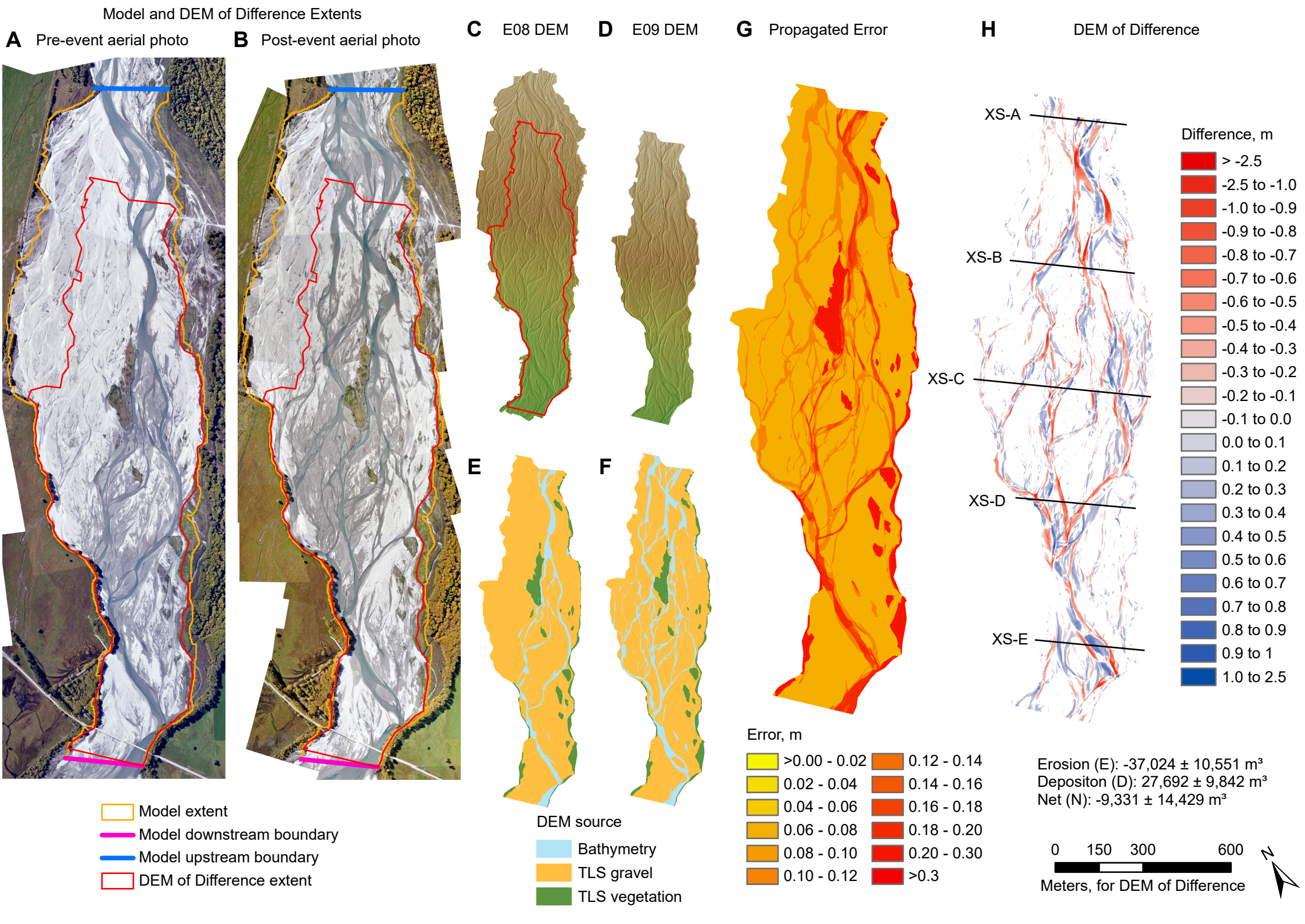
Model and DEM of Difference Extents
A Pre-event aerial photo
B Post-event aerial photo
C E08 DEM
D E09 DEM
E
F
G Propagated Error
H DEM of Difference
XS-A
XS-B
XS-C
XS-D
XS-E
Difference, m
> -2.5
-2.5 to -1.0
-1.0 to -0.9
-0.9 to -0.8
-0.8 to -0.7
-0.7 to -0.6
-0.6 to -0.5
-0.5 to -0.4
-0.4 to -0.3
-0.3 to -0.2
-0.2 to -0.1
-0.1 to 0.0
0.0 to 0.1
0.1 to 0.2
0.2 to 0.3
0.3 to 0.4
0.4 to 0.5
0.5 to 0.6
0.6 to 0.7
0.7 to 0.8
0.8 to 0.9
0.9 to 1
1.0 to 2.5
Model extent
Model downstream boundary
Model upstream boundary
DEM of Difference extent
DEM source
Bathymetry
TLS gravel
TLS vegetation
Error, m
>0.00 - 0.02
0.02 - 0.04
0.04 - 0.06
0.06 - 0.08
0.08 - 0.10
0.10 - 0.12
0.12 - 0.14
0.14 - 0.16
0.16 - 0.18
0.18 - 0.20
0.20 - 0.30
>0.3
Erosion (E): -37,024 ± 10,551 m³
Depositon (D): 27,692 ± 9,842 m³
Net (N): -9,331 ± 14,429 m³
0
150
300
600
Meters, for DEM of Difference
N

Figure 2. Figure

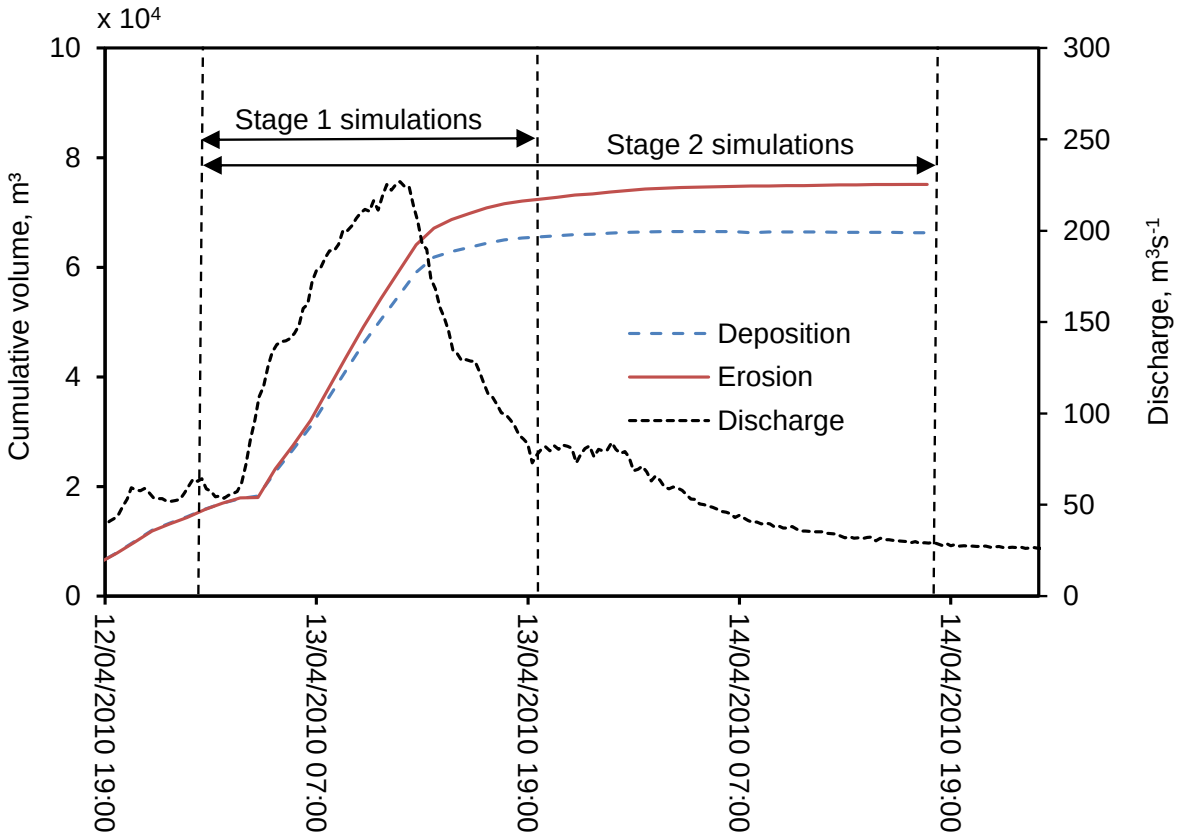
x 10⁴
10
8
6
4
2
0
300
250
200
150
100
50
0
Cumulative volume, m³
Discharge, m³s⁻¹
Stage 1 simulations
Stage 2 simulations
Deposition
Erosion
Discharge
12/04/2010 19:00
13/04/2010 07:00
13/04/2010 19:00
14/04/2010 07:00
14/04/2010 19:00

Figure 3. Figure

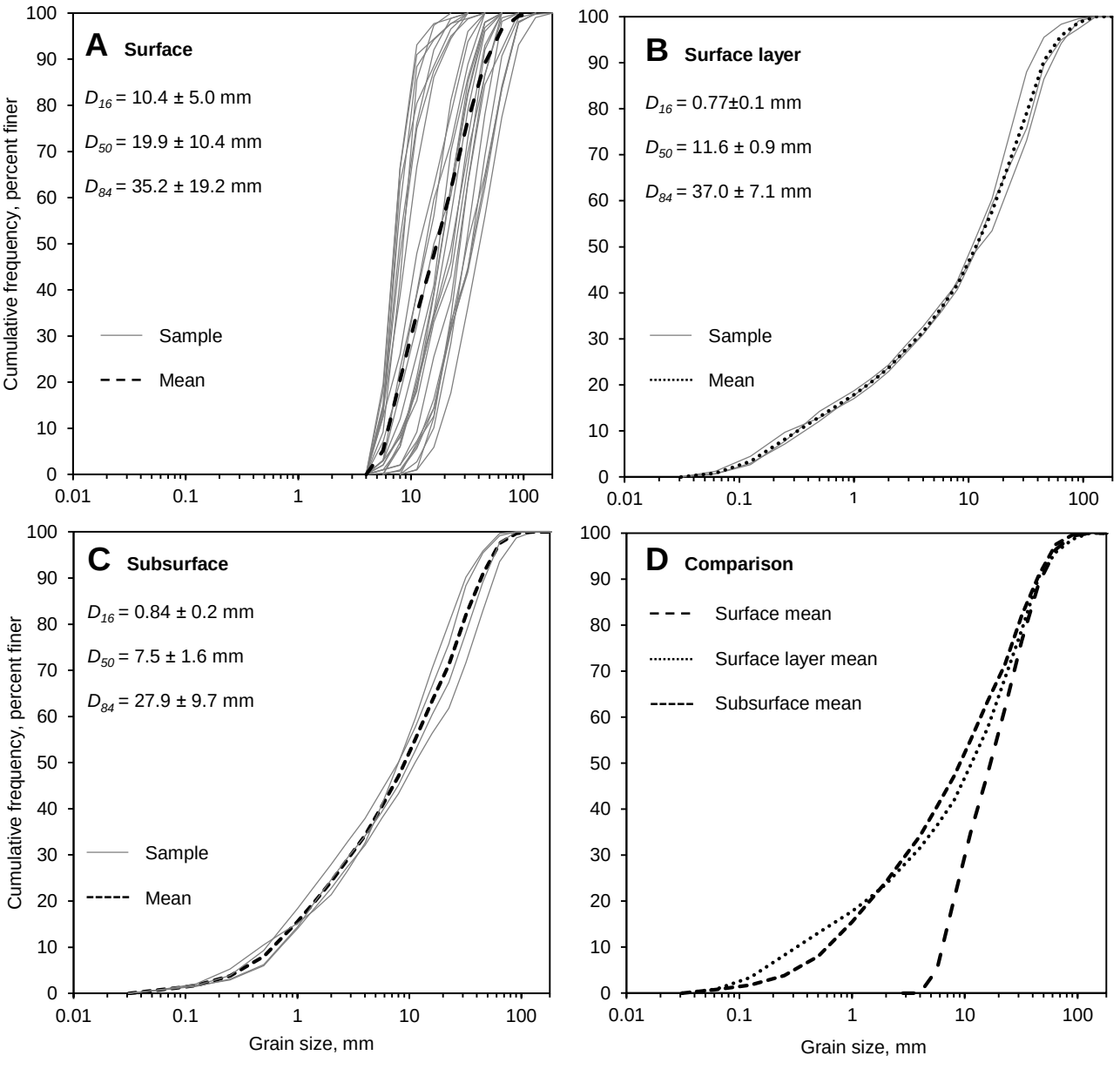
A Surface
D_{16} = 10.4 ± 5.0 mm
D_{50} = 19.9 ± 10.4 mm
D_{84} = 35.2 ± 19.2 mm
Sample
Mean
B Surface layer
D_{16} = 0.77±0.1 mm
D_{50} = 11.6 ± 0.9 mm
D_{84} = 37.0 ± 7.1 mm
Sample
Mean
C Subsurface
D_{16} = 0.84 ± 0.2 mm
D_{50} = 7.5 ± 1.6 mm
D_{84} = 27.9 ± 9.7 mm
Sample
Mean
D Comparison
Surface mean
Surface layer mean
Subsurface mean
Cumulative frequency, percent finer
Grain size, mm
0.01
0.1
1
10
100
0
10
20
30
40
50
60
70
80
90

Figure 4. Figure

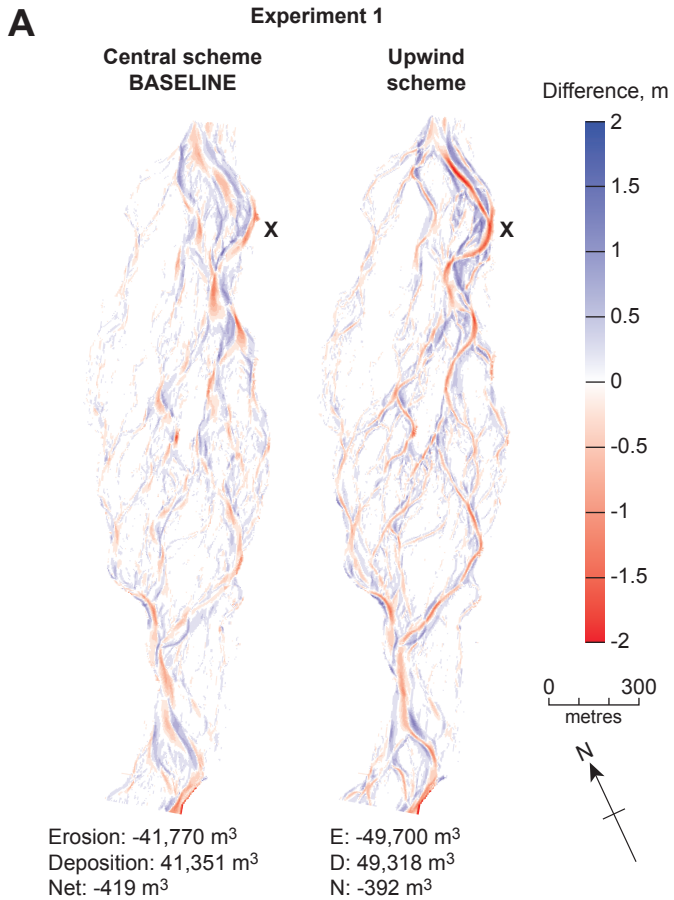
A
Experiment 1
Central scheme
BASELINE
Upwind
scheme
Difference, m
2
1.5
1
0.5
0
-0.5
-1
-1.5
-2
X
X
0
300
metres
N
Erosion: -41,770 m3
Deposition: 41,351 m3
Net: -419 m3
E: -49,700 m3
D: 49,318 m3
N: -392 m3

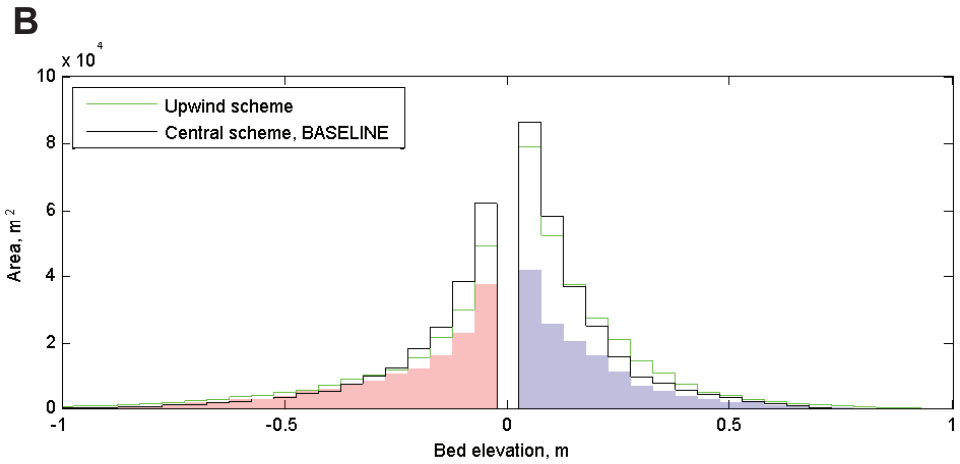
B
x 10^4
10
8
6
4
2
0
Upwind scheme
Central scheme, BASELINE
Area, m^2
-1
-0.5
0
0.5
1
Bed elevation, m

Figure 5. Figure

BASELINE
Q = Gauge
d_{min} = 0.10 m

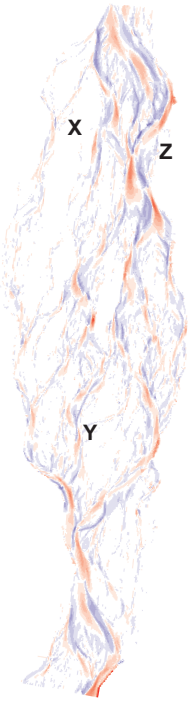

Erosion: -41,770 m³
Deposition: 41,351 m³
Net: -419 m³

Experiment 2a
No helical flow

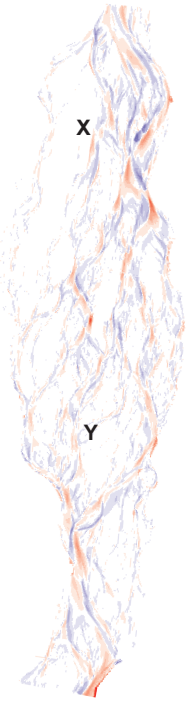

E: -36,621 m³
D: 36,681 m³
N: 60 m³

Experiment 2b
k_S = 0.03 m

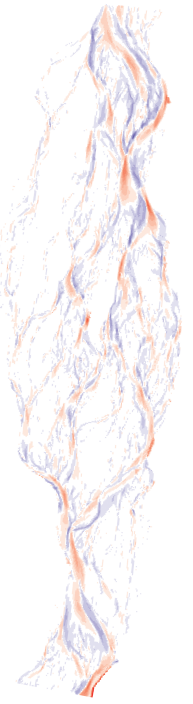

E: -39,935 m³
D: 39,495 m³
N: -440 m³

k_S = 0.05 m

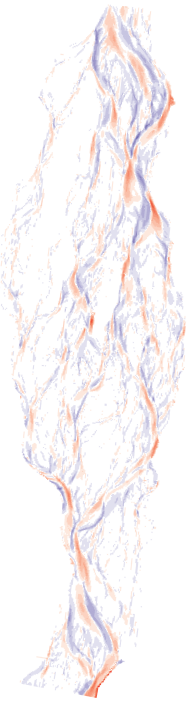

E: -43,903 m³
D: 43,538 m³
N: -365 m³

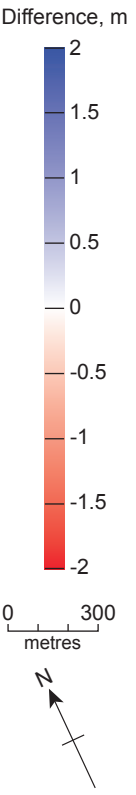

Experiment 2c
ν_H = 1.0 m²s⁻¹

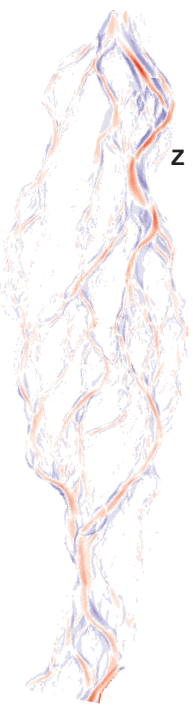

E: -38,310 m³
D: 36,590 m³
N: -1,720 m³

Experiment 2d
Q = Gauge -15%

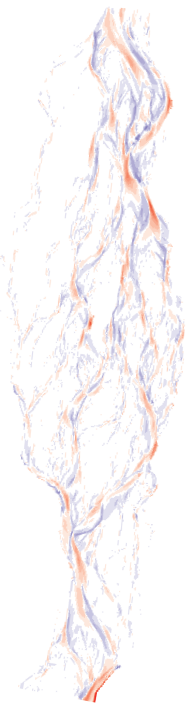

E: -36,236 m³
D: 35,344 m³
N: -892 m³

Q = Gauge +15%

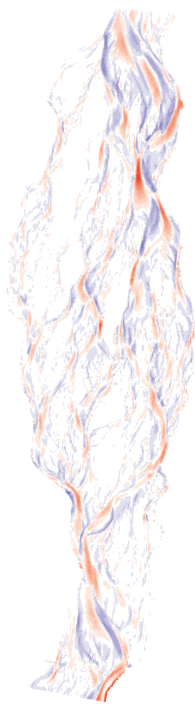

E: -47,555 m³
D: 47,565 m³
N: 10 m³

Experiment 2e
d_{min} = 0.05 m

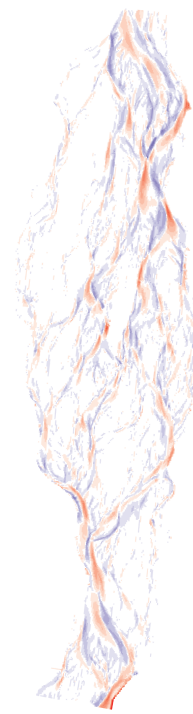

E: -42,258 m³
D: 41,879 m³
N: -379 m³

Figure 6. Figure

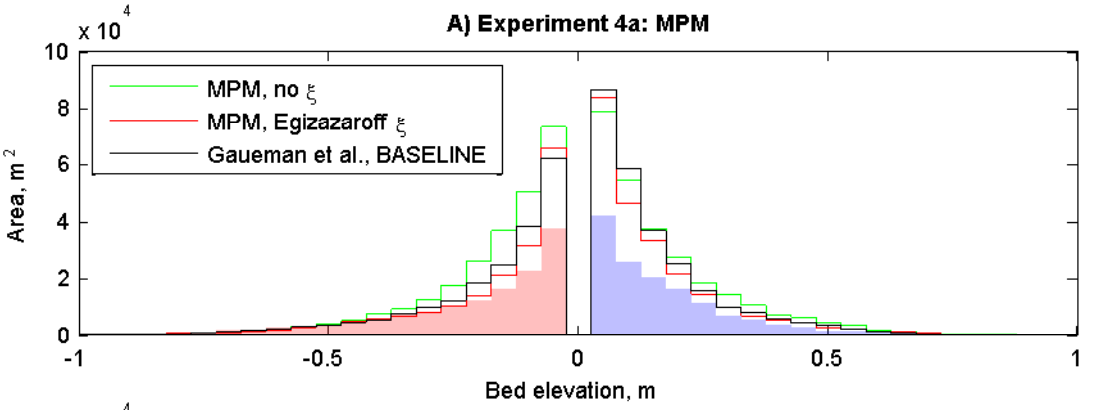
A) Experiment 4a: MPM
x 10^4
MPM, no ξ
MPM, Egizazaroff ξ
Gaueman et al., BASELINE
Area, m^2
Bed elevation, m

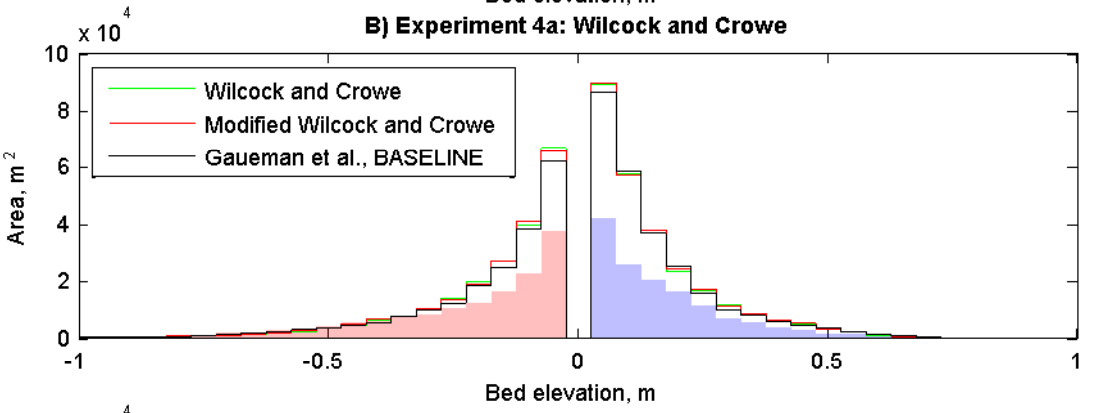
B) Experiment 4a: Wilcock and Crowe
x 10^4
Wilcock and Crowe
Modified Wilcock and Crowe
Gaueman et al., BASELINE
Area, m^2
Bed elevation, m

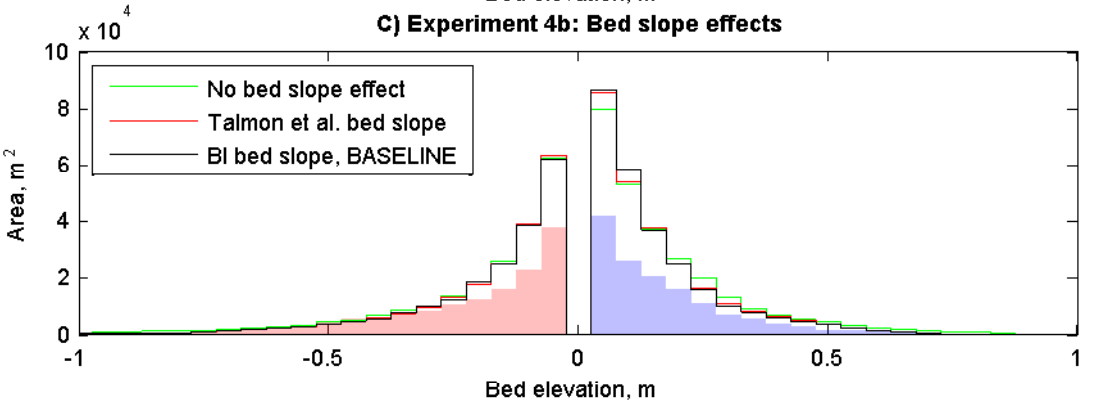
C) Experiment 4b: Bed slope effects
x 10^4
No bed slope effect
Talmon et al. bed slope
Bl bed slope, BASELINE
Area, m^2
Bed elevation, m

Figure 7. Figure

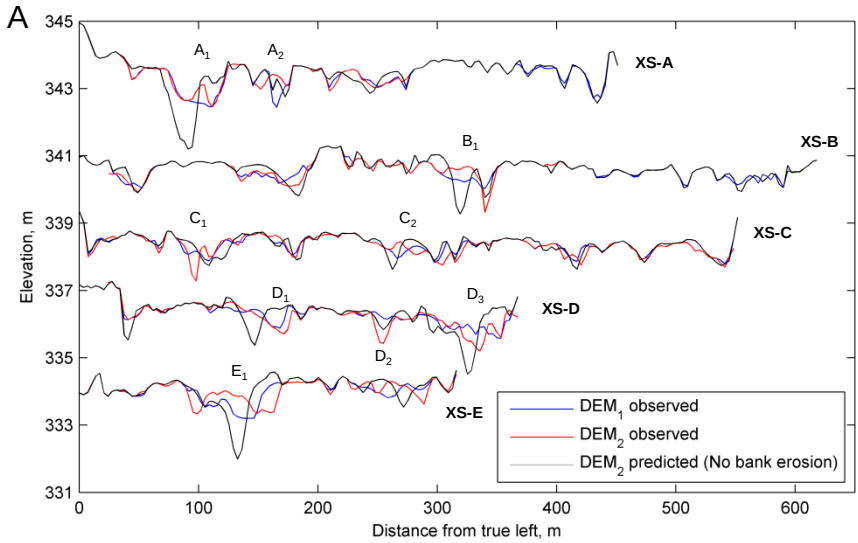
A
Elevation, m
Distance from true left, m
A1
A2
B1
C1
C2
D1
D2
D3
E1
XS-A
XS-B
XS-C
XS-D
XS-E
DEM1 observed
DEM2 observed
DEM2 predicted (No bank erosion)

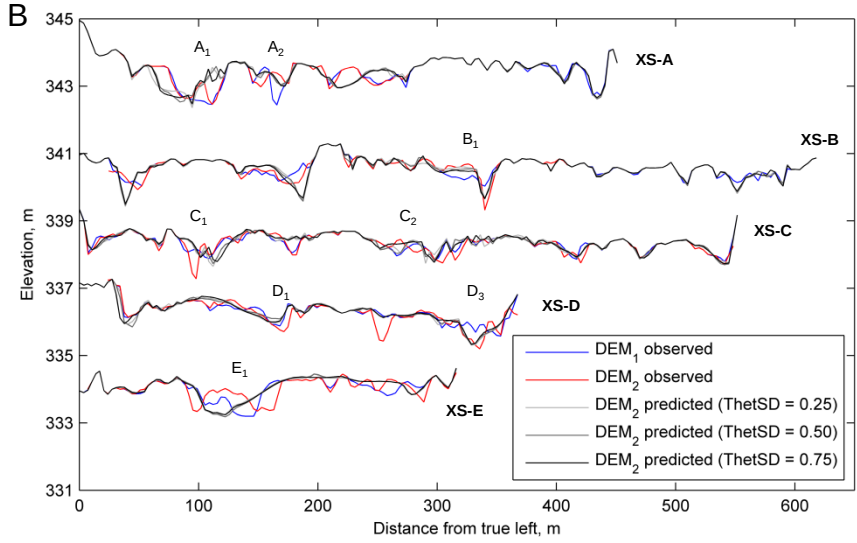
B
Elevation, m
Distance from true left, m
A1
A2
B1
C1
C2
D1
D3
E1
XS-A
XS-B
XS-C
XS-D
XS-E
DEM1 observed
DEM2 observed
DEM2 predicted (ThetSD = 0.25)
DEM2 predicted (ThetSD = 0.50)
DEM2 predicted (ThetSD = 0.75)

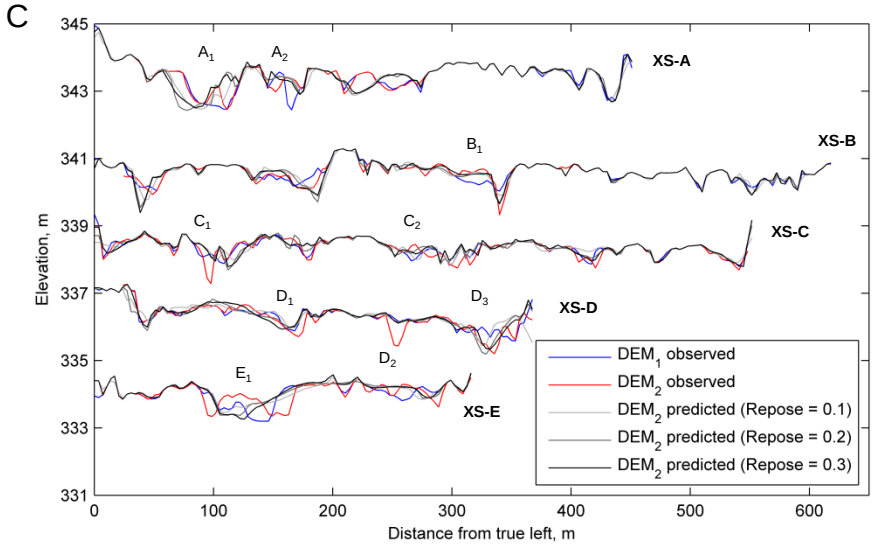
C
Elevation, m
Distance from true left, m
A1
A2
B1
C1
C2
D1
D2
D3
E1
XS-A
XS-B
XS-C
XS-D
XS-E
DEM1 observed
DEM2 observed
DEM2 predicted (Repose = 0.1)
DEM2 predicted (Repose = 0.2)
DEM2 predicted (Repose = 0.3)

Figure 8. Figure

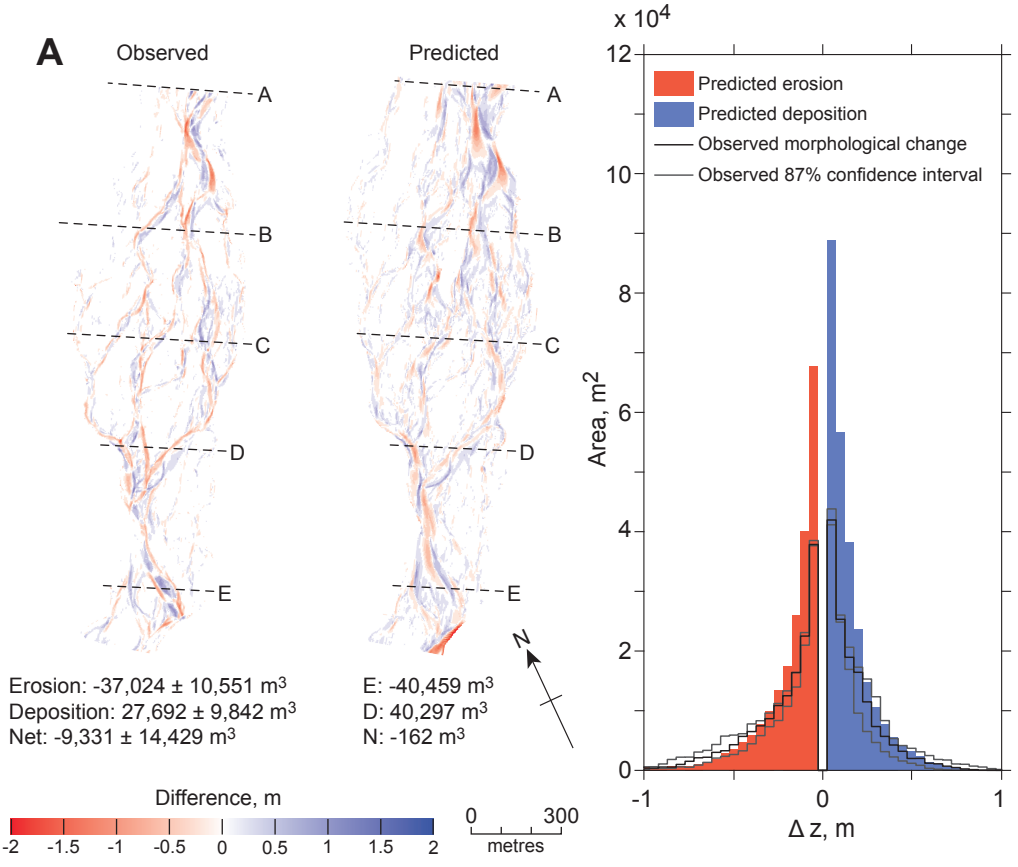
A
Observed
Predicted
A
B
C
D
E
Erosion: -37,024 ± 10,551 m3
Deposition: 27,692 ± 9,842 m3
Net: -9,331 ± 14,429 m3
E: -40,459 m3
D: 40,297 m3
N: -162 m3
N
Difference, m
-2 -1.5 -1 -0.5 0 0.5 1 1.5 2
0 300
metres
x 10^4
Predicted erosion
Predicted deposition
Observed morphological change
Observed 87% confidence interval
Area, m2
Δ z, m

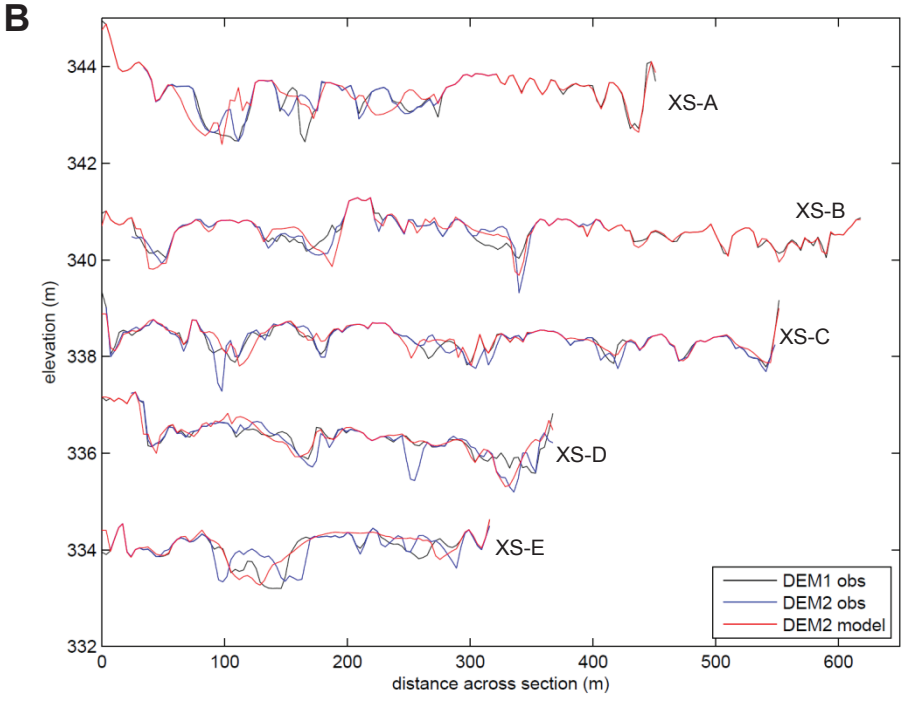
B
XS-A
XS-B
XS-C
XS-D
XS-E
elevation (m)
distance across section (m)
DEM1 obs
DEM2 obs
DEM2 model